AD-766 084

UNSTEADY FLUID DYNAMIC RESPONSE OF AN AXIAL-FLOW COMPRESSOR STAGE WITH DISTORTED INFLOW

John J. Adamczyk, et al

Purdue University

Prepared for:

Office of Naval Research

July 1973

DISTRIBUTED BY:

NTIS

National Technical Information Service
U. S. DEPARTMENT OF COMMERCE
5285 Port Royal Road, Springfield Va. 22151

AD 766084

PROJECT SQUID

TECHNICAL REPORT UARL-2-PU

UNSTEADY FLUID DYNAMIC RESPONSE OF AN AXIAL-FLOW COMPRESSOR STAGE WITH DISTORTED INFLOW

BY

JOHN J. ADAMCZYK
and
FRANKLIN O. CARTA
UNITED AIRCRAFT RESEARCH LABORATORIES
EAST HARTFORD, CONNECTICUT

PROJECT SQUID HEADQUARTERS
THERMAL SCIENCE AND PROPULSION CENTER
PURDUE UNIVERSITY
WEST LAFAYETTE, INDIANA 47907

D D C
SEP 10 1973
B

JULY 1973

Project SQUID is a cooperative program of basic research relating to Jet Propulsion. It is sponsored by the Office of Naval Research and is administered by Purdue University through Contract N00014-67-A-0226-0005, NR-098-038.

This document has been approved for public release and sale, its distribution is unlimited

NATIONAL TECHNICAL INFORMATION SERVICE

Unclassified
Security Classification

DOCUMENT CONTROL DATA - R & D

(Security classification of title, body of abstract and indexing annotation must be entered when the overall report is classified)

1. ORIGINATING ACTIVITY (Corporate author)
Project SQUID, Thermal Science and Propulsion Center
Purdue University, West Lafayette, Indiana 47907

2a. REPORT SECURITY CLASSIFICATION
Unclassified

2b. GROUP
N/A

3. REPORT TITLE
Unsteady Fluid Dynamic Response of an Axial-Flow Compressor Stage with Distorted Inflow

4. DESCRIPTIVE NOTES (Type of report and inclusive dates)
Technical Report

5. AUTHOR(S) (First name, middle initial, last name)
John J. Adamczyk and
Franklin O. Carta

6. REPORT DATE
July 1973

7a. TOTAL NO. OF PAGES
65

7b. NO. OF REFS
13

8a. CONTRACT OR GRANT NO.
N00014-67-A-0226-0005

b. PROJECT NO.
NR-098-038

c.

d.

9a. ORIGINATOR'S REPORT NUMBER(S)
UARL-2-PU

9b. OTHER REPORT NO(S) (Any other numbers that may be assigned this report)
UARL Report M911103-7

10. DISTRIBUTION STATEMENT
This document has been approved for public release and sale; its distribution is unlimited.

11. SUPPLEMENTARY NOTES
None

12. SPONSORING MILITARY ACTIVITY
Office of Naval Research, Power Program, Code 473, Department of the Navy, Arlington, Virginia 22217

13. ABSTRACT

A nonlinear, large disturbance theory has been developed which couples, interactively, the flow through the blade passages of a turbomachine blade row and an axially distorted flow field. The blade row analysis is based on the time-dependent energy equation of the flow through the passage and includes a nonlinear description of cascade loss and turning correlations from available experimental sources. The flow field analysis involves the nonlinear, time-dependent equations for the vorticity and the stream function. Coupling of the two is accomplished through the boundary conditions by mutual relationships between the pressure change across the blade row and the change in vorticity in the flow field analyses.

Within the assumptions that the flow is two-dimensional and incompressible, the numerical solution is capable of predicting the influence of an upstream axial distortion on the onset of a circumferentially rotating stall pattern for a single blade row. The speed of rotation of the stall cell and the spatial attenuation of the distortion wave are also predicted, and although the observed experimental data are generally available only for multistage systems, the predicted results for the single blade row are in qualitively good agreement with the data.

The two major parts of the theory can be decoupled and the blade row analysis can be performed separately. For a prescribed axial distortion measured at the blade row inlet face, this portion of the theory predicts a circumferential pressure distribution at the blade row exit which is in good agreement with measured exit data.

DD FORM 1 NOV 65 1473 (PAGE 1)
S/N 0101-807-6801

Unclassified
Security Classification

14 KEY WORDS	LINK A ROLE	LINK A WT	LINK B ROLE	LINK B WT	LINK C ROLE	LINK C WT
Inlet distortion analysis						
Compressor response to stationary inlet distortion						
Rotating stall prediction						
Circumferential distortion						
Unsteady fluid dynamic analysis						

United Aircraft Research Laboratories

UNITED AIRCRAFT CORPORATION

EAST HARTFORD, CONNECTICUT 06108

Project SQUID Technical Report UARL-2-PU

UNSTEADY FLUID DYNAMIC RESPONSE
OF AN AXIAL-FLOW COMPRESSOR STAGE
WITH DISTORTED INFLOW

Work performed under Contract No. 4965-32
for Project SQUID (Subcontract under
ONR Contract N00014-67-0226-0005,
NR-098-038).

REPORTED BY John J. Adamczyk

Franklin O. Carta

APPROVED BY Marvin C. Cheney, Jr., Chief
Aerodynamics Section

DATE July 1973

TABLE OF CONTENTS

	Page
SUMMARY	1
INTRODUCTION	3
BLADE ROW ANALYSIS	7
APPLICATION OF BLADE ROW ANALYSIS	14
TWO-DIMENSIONAL FLOW FIELD ANALYSIS	17
NUMERICAL PROCEDURE AND BOUNDARY CONDITIONS	22
Inlet Conditions	22
Flow Periodicity	23
Pressure Rise Across Actuator Disk	24
Vorticity at Blade Row Exit Plane	25
Flow Field at Exit Plane	25
COUPLED FLOW FIELD AND BLADE ROW ANALYSIS	26
RESULTS AND CONCLUSIONS	32
REFERENCES	34
LIST OF SYMBOLS	36
FIGURES	38

Unsteady Fluid Dynamic Response of an Axial-Flow Compressor Stage with Distorted Inflow

SUMMARY

A nonlinear, large disturbance theory has been developed which couples, interactively, the flow through the blade passages of a turbomachine blade row and an axially distorted flow field. The blade row analysis is based on the time-dependent energy equation of the flow through the passage and includes a nonlinear description of cascade loss and turning correlations from available experimental sources. The flow field analysis involves the nonlinear, time-dependent equations for the vorticity and the stream function. Coupling of the two is accomplished through the boundary conditions by mutual relationships between the pressure change across the blade row and the change in vorticity in the flow field analyses.

Within the assumptions that the flow is two-dimensional and incompressible, the numerical solution is capable of predicting the influence of an upstream axial distortion on the onset of a circumferentially rotating stall pattern for a single blade row. The speed of rotation of the stall cell and the spatial attenuation of the distortion wave are also predicted, and although the observed experimental data are generally available only for multistage systems, the predicted results for the single blade row are in qualitively good agreement with the data.

The two major parts of the theory can be decoupled and the blade row analysis can be performed separately. For a prescribed axial distortion measured at the blade row inlet face, this portion of the theory predicts a circumferential pressure distribution at the blade row exit which is in good agreement with measured exit data.

INTRODUCTION

At its inception the object of this program was to assess the extent to which the performance characteristics of a compressor operating in a circumferentially distorted inlet flow are influenced by unsteady aerodynamic effects. A first effort (Ref. 1) concentrated on the development of an unsteady model based on unsteady aerodynamic data from an isolated airfoil, and it was shown that a reasonable correlation could be attained between measured and predicted circumferential pressure variations. Although this model yielded encouraging results it was recognized that it depended strongly on a number of intermediate transformations and assumptions to convert isolated airfoil data to a form compatible with compressor operation. A more serious limitation of the model in Ref. 1 involved the use of measured upstream flow properties obtained at the inlet plane during an inlet distortion experiment. These upstream conditions are strongly dependent on the presence of the blade row, as shown in Fig. 1. Here the measured stall angle parameter, σ , has been plotted versus circumferential position, θ , for a 180 deg distortion condition analyzed in Ref. 1. The dashed line in Fig. 1 represents the angle of attack distribution that would be measured immediately behind the distortion screen far upstream of the blade row, and the solid line is the actual angle of attack distribution at the blade row inlet. It is seen that the mutual interaction between the blade row and the circumferential velocity profile far upstream of the blade row produces a further

distortion of large magnitude on the previously distorted flow. However, at the conclusion of the work reported in Ref. 1 it was not possible to predict the change in the distortion pattern as it came under the influence of the blade row, and it was necessary to measure the upstream conditions during an actual distortion experiment.

One of the principal objectives of the present work is to provide the engine designer with the analytical means to estimate the distortion tolerance or the distorted flow performance of a rotor, including unsteady effects, without resorting to an expensive test program. This means the designer must be able to prescribe a distortion far upstream of the rotor face, and the analysis must be capable of properly modifying the distortion at the rotor face in accordance with the coupling between the upstream flow distortion and the downstream boundary conditions.

It was just shown (cf. Fig. 1) that the coupling between the downstream flow and the upstream distortion is quite strong, and it is not possible to prescribe the conditions at the compressor face a priori on the basis of upstream distortion profile and geometry alone. Hence an effort was made to derive an analytical method to predict the behavior of the entire coupled flow field. Several analyses (Refs. 2, 3, 4) have attempted to do this using linearized theory (based on the assumption of a small disturbance compared to the mean velocity). However, this restriction is inappropriate for the inlet distortion problem which has large amplitude flow fluctuations which could cause the compressor to operate beyond the steady-state stall

boundary over a significant circumferential sector. Accordingly, the present method involves a numerical solution of a set of nonlinear equations which are not restricted by a small disturbance requirement, and which account for the interactive influences of the blade row and the entire distorted flow field.

In particular, the present stability analysis was initially divided into two parts which modelled the blade row and the flow field separately. By this means it was possible to demonstrate the validity (and tractability) of each constituent part before attempting to couple them in a single stability analysis.

In the first part the earlier blade row model of Ref. 1 was replaced with a more direct representation which accounted for the presence of neighboring blades. This new model describes the unsteady flow through a blade passage of either a rotor or a stator blade row. It is based on the time-dependent energy equation of the flow through the passage and includes a nonlinear description of cascade loss and turning correlations from available experimental sources. Use of this model with prescribed upstream conditions at the blade row inlet plane yielded good agreement with measured data.

The second part of the present analysis was concerned with developing a flow field model for the regions upstream and downstream of the blade row. This model was designed to be capable of accounting for mutual interactions between the blade row and the upstream inlet distortion. This part consists

of a nonlinear, two-dimensional, time dependent flow field analysis involving the equations for the vorticity and the stream function. Initially this flow field solution was decoupled from the blade row analysis to provide a baseline transient response problem suitable for checking out the stability of the required numerical procedures.

Finally, the two parts of the analysis were coupled. The upstream and downstream flow transients contributed to the time-dependent blade passage flows, and the unsteady blade row pressure rise provided a mid-flow boundary condition for the time-dependent flow field analysis. Direct comparisons with experiment were not made because of the lack of experimental data on the response of an isolated rotor subjected to an upstream distortion. Nevertheless, it is felt that the results show reasonable trends which are qualitatively correct when compared with available experimental data for a multi-stage compressor.

BLADE ROW ANALYSIS

Consider the flow of an incompressible fluid through one of the blade passages shown in Fig. 2. The flow is assumed to be two-dimensional, and it enters the passage at station 1 and exits at station 2. Continuity requires that the flow which exists at station 2 must be equal to the flow entering at station 1. This can be expressed by the equation

$$\int_{y_a}^{y_d} U_1 dy = \bar{U}_1 \tau = \int_{y_b}^{y_c} U_2 dy = \bar{U}_2 \tau \equiv Q \tag{1}$$

where Q is the flow rate through the passage, and the bar over the variables U_1 and U_2 denotes gap-averaged quantities. Thus, the continuity equation requires that the average axial velocity be a constant at every point within the blade passage

$$\bar{U}_1 = \bar{U}_2 = U \tag{2}$$

In the present problem the flow through each blade passage is, in general, unsteady. Hence the accompanying variation in energy flux through each passage will be accounted for using the unsteady energy equation for an incompressible fluid (cf. Eq. (2.21) in Ref. 5) flowing through a control volume. When this equation is rewritten in the present notation we obtain

$$\int_V \frac{\partial}{\partial t}\left(\frac{1}{2}\rho q^2\right) dv + \oint_{abcda} \left(\frac{p}{\rho} + \frac{1}{2}q^2\right)\rho\, \vec{q}\cdot\hat{n}\, dA = 0 \tag{3}$$

where v in the first integral denotes the control volume and the notation abcda under the line integral denotes the control surface in Fig. 2 over which it is to be evaluated. The line integrals along the airfoils, ab and cd, are zero because the flow is everywhere tangent to these surfaces, so $\vec{q}\cdot\vec{n}dA = 0$. The remaining integrals over bc and da may be simplified by using

$$\left.\begin{aligned}\vec{q}_1\cdot\vec{n}\,dA &= -U_1 dy\\ \vec{q}_2\cdot\vec{n}\,dA &= U_2 dy\end{aligned}\right\} \tag{4}$$

so Eq. (1) becomes

$$\int_{y_b}^{y_c}\left(p_2+\frac{1}{2}\rho q_2^2\right)U_2 dy-\int_{y_a}^{y_d}\left(p_1+\frac{1}{2}\rho q_1^2\right)U_1 dy+\int_v\frac{\partial}{\partial t}\left(\frac{1}{2}\rho q^2\right)dv=0 \tag{5}$$

Bernoulli's equation may now be used to replace the sum of the static and dynamic pressures at the inlet and exit planes by total pressures,

$$\int_{y_b}^{y_c} P_{02}U_2 dy-\int_0^{\tau}P_{01}U_1\,dy=-\int_v\frac{\partial}{\partial t}\left(\frac{1}{2}\rho q^2\right)dv \tag{6}$$

The validity of the next portion of this analysis depends on our ability to perform meaningful gap averages of many of the variables. Inherent in this requirement is the concurrent requirement that these variables be, in general, slowly varying circumferentially with wavelengths that are greater than blade gap. Under these conditions the variable will simply be replaced by its local value. For example, if both the inlet total pressure and the inlet velocity meet this requirement, the second integral in Eq. (6) may be

rewritten as

$$\int_0^{\tau} P_{01} U_1 dy \cong P_{01} U \tau = P_{01} Q \tag{7}$$

If the assumption of no losses in the flow were made, the same result would be obtained for the first integral in Eq. (6). Instead, it will be assumed that a total pressure loss occurs that is associated with blade wakes and P_{02} and U_2 will be replaced by $\overline{P}_{02} + \Delta P_{02}$ and $\overline{U}_2 + \Delta U_2$, respectively. Here the bar represents the gap average of a quantity which varies rapidly in a local region, such as the wake, but which has an otherwise slowly varying characteristic. The variables ΔP_{02} and ΔU_2 are local deviations from the gap-averaged quantities and represent some measure of the loss, to be resolved in the analysis below. The first integral of Eq. (6) will now be replaced by

$$\int_{y_b}^{y_c} P_{02} U_2 dy = \int_{y_b}^{y_c} (\overline{P}_{02} + \Delta P_{02})(\overline{U}_2 + \Delta U_2) dy = \overline{P}_{02} \overline{U}_2 \tau + \int_{y_b}^{y_c} \Delta P_{02} \Delta U_2 dy$$

$$\equiv \overline{P}_{02} \overline{U}_2 \tau + \frac{1}{2} \rho q_1^2 X \overline{U}_2 \tau \tag{8}$$

$$= \overline{P}_{02} Q + \frac{1}{2} \rho q_1^2 X Q$$

where X is an unsteady loss parameter (see below).

The unsteady loss parameter, X, is conceptually defined in Eqs. (8) as the instantaneous gap-averaged deviation of exit total pressure during an

unsteady process. In a steady-state process a combination of Eqs. (6), (7), and (8) shows that X reverts to its traditional steady-state definition,

$$X_{ss} = \frac{P_{01} - \bar{P}_{02}}{\frac{1}{2}\rho q_1^2} \tag{9}$$

Although the specific unsteady behavior of X is not known, experience has shown that unsteady processes do not follow the steady characteristics, but lag them by some appropriate time constant. Consequently, a hypothetical first order lag model will be chosen, as in Refs. 6 and 7,

$$\frac{c_{ax}\alpha_T}{U^*}\frac{\partial X}{\partial t} + X = X_{ss} \tag{10}$$

where α_T is a dimensionless time constant associated with the chordwise convection of disturbances within the boundary layer and where U* is the circumferential average of the axial velocity,

$$U^* = \frac{1}{2\pi}\int_0^{2\pi} U\,d\theta \tag{11}$$

(Note that θ and y are both tangential coordinates.) This hypothetical model will be used presently.

Consider next the rate of change of kinetic energy within the passage, represented by the right hand side of Eq. (6). The square of the local

velocity can be rewritten as

$$q^2 = U^2 + V^2 = U^2(1 + \tan^2\xi) = U^2\sec^2\xi \tag{12}$$

where $\xi(x,y,t)$ is the local flow angle within the passage. Hence, the volume integral becomes

$$\int_v \frac{\partial}{\partial t}\left(\frac{1}{2}\rho q^2\right) dv = \frac{1}{2}\rho \frac{\partial}{\partial t}\int_0^{c_{ax}}\int_{y_1(x)}^{y_2(x)} U^2\sec^2\xi \, dy\, dx \tag{13}$$

where $y_1(x)$ and $y_2(x)$ are the y-coordinates of blades ab and dc, respectively (cf. Fig. 2). The evaluation of this integral depends on a number of assumptions. First it is assumed that the flow within each passage is mostly one-dimensional. In other words, the assumption is made that variations normal to the mean streamline through the passage are small, which implies that separate gap averages of the integrand factors can be taken, or

$$\int_0^{c_{ax}}\int_{y_1(x)}^{y_2(x)} U^2\sec^2\xi \, dy\, dx = \tau\int_0^{c_{ax}} \overline{U^2}\;\overline{\sec^2\xi}\, dx \tag{14}$$

From above, $\overline{U}$ is independent of x through the blade passage. Furthermore, it will be assumed that $\overline{U}$ is slowly varying in the circumferential direction, and in accordance with the convention established earlier, the gap-averaged $\overline{U}$ will be replaced by its local value. Hence, $\overline{U^2} \cong \overline{U}^2 \cong U^2$ which can be

removed from under the x-integral in Eq. (13), which now becomes

$$\int_v \frac{\partial}{\partial t}\left(\frac{1}{2}\rho q^2\right) dv = \frac{1}{2}\rho\tau \frac{\partial}{\partial t} U^2 \int_0^{c_{ax}} \overline{\sec^2 \xi}\, dx \tag{15}$$

Finally, the assumption of small gap to chord ratio will be made. Under this assumption virtually all of the flow angle changes will take place in the entrance region of each passage, the chordwise extent of which is small compared with the chord, and the flow through the remainder of each passage will behave like a channel flow (Ref. 8). Hence, the chordwise integral of $\overline{\sec^2 \xi}$ in Eq. (15) can be replaced by

$$\int_0^{c_{ax}} \overline{\sec^2 \xi}\, dx \cong \int_0^{c_{ax}} \sec^2 \xi_{metal}\, dx \equiv c_{ax} \Xi_m \tag{16}$$

where ξ_{metal} is the angle of the blade camber line, commonly called the metal angle, and where Ξ_m now represents a chordwise average. Furthermore, this quantity is independent of time by virtue of its channel-like behavior, so Eq. (15) becomes

$$\int_v \frac{\partial}{\partial t}\left(\frac{1}{2}\rho q^2\right) dv = \frac{1}{2}\rho\tau\, c_{ax}\Xi_m \times 2U \frac{\partial U}{\partial t} = \rho Q c_{ax} \Xi_m \frac{\partial U}{\partial t} \tag{17}$$

When Eqs. (7), (8), and (17) are substituted into Eq. (6) the result is

$$\bar{P}_{02} - P_{01} = \Delta P_0 = -\frac{1}{2}\rho q_1^2 \chi - \rho\, c_{ax} \Xi_m \frac{\partial U}{\partial t} \tag{18}$$

(which is equivalent to Eq. (9) in Ref. 7). Once again Bernoulli's equation will be used at both inlet and exit planes,

$$\left.\begin{aligned} P_{01} &= p_1 + \tfrac{1}{2}\rho q_1^2 \\ \bar{P}_{02} &= p_2 + \tfrac{1}{2}\rho q_2^2 \end{aligned}\right\} \tag{19}$$

Here a specific notation for gap averaging is not necessary on p_2 because in the definition of $\bar{P}_{02}$ (Eqs. (8)) all of the local wake deficiencies have been lumped together in the loss parameter, χ. Hence, both p_2 and q_2 can be regarded as slowly varying quantities and can be represented by local values. It was stated earlier that the equation of continuity requires that the gap-averaged axial velocity, U, be constant through the blade row. Thus we may write

$$U = q_1 \sin\beta_1 = q_2 \sin\beta_2 \tag{20}$$

Again, no specific gap averaging notation is necessary for β_2 because its value will be taken from a set of gap-averaged correlation results such as those in Ref. 9. With the introduction of Eqs. (19) and (20), Eq. (18) now becomes

$$p_2 = p_1 + \tfrac{1}{2}\rho q_1^2\left(1 - \frac{\sin^2\beta_1}{\sin^2\beta_2}\right) - \tfrac{1}{2}\rho q_1^2 \chi - \rho c_{0x} \Xi_m \frac{\partial U}{\partial t} \tag{21}$$

APPLICATION OF BLADE ROW ANALYSIS

Before the blade row analysis was coupled with the flow field analysis (see subsequent sections below) it was decided to test its validity by using it to examine some of the experimental data previously analyzed in Ref. 1. In this application the measured inlet conditions at the rotor face were prescribed to determine rotor exit conditions, and the measured inlet conditions at the stator face (i.e., the rotor exit conditions) were prescribed to determine stator exit conditions. All of the quantities on the right hand side of Eq. (21) were known or easily derived. For example, steady-state loss and turning characteristics for the rotor and stator had been previously determined experimentally and are shown in Fig. 3 versus inlet angle, β_1. The time derivative in Eq. (21) was rewritten in terms of rotor rotation speed, $\partial/\partial t = \Omega\partial/\partial\theta$, and the loss coefficient time constant in Eq. (10) was assigned the value $\alpha\tau = 1$, in accordance with the measurements of Ref. 10. The inlet angle, β_1, was then determined as a function of circumferential position, θ, and Eq. (10) was solved for $X(\theta)$ using $X_{ss}(\beta_1(\theta))$ as a known input. Finally, the exit static pressures were calculated for both rotor and stator using Eq. (21).

Three specific cases for 180 deg circumferential screens from Ref. 1 were examined and are presented in Figs. 4, 5, and 6 for the mid flow, peak pressure, and surge conditions, respectively (cf. Figs. 18, 9, and 22 of Ref. 1). In each of these figures the square, triangular, and circular

symbols denote measured rotor inlet, rotor exit, and stator exit pressures. The solid curves are the exit pressures predicted by Eq. (21). A comparison with the results in Ref. 1 showed that Eq. (21) generally improved the correlation with the experimental data. This is particularly true in the prediction of the rotor exit pressure for the peak pressure condition as shown in Fig. 7.

The apparent discrepancies for the stator prediction in all three cases can be ascribed to a general inadequacy of the steady-state stator performance data which had to be extrapolated to encompass the unsteady operating limits during distorted operation. The disagreement between predicted and measured rotor pressure in Fig. 6 at the screen exit ($\theta \cong 90$ deg) is also believed to be ascribable in part to a required extrapolation of rotor performance data. More importantly, the combination of deep stall penetration and unsteady flow at the screen edge probably caused a flow instability that was not measureable in detail with the steady-state instrumentation used in this experiment. Furthermore, use of Eq. (21) with spatially fixed input variables can only yield spatially fixed exit predictions, and it will be shown in a later section that a coupling between the flow field equations and Eq. (21) leads to both temporal and spatial flow instabilities under conditions of deep stall penetration. Consequently it was felt that most of the observed discrepancies in Figs. 4, 5, and 6 could be discounted, and that the agreement between rotor exit pressure prediction and experiment, shown in Fig. 5, was significant and provided the required validation of Eq. (21).

A closer examination of the effects of individual terms in Eq. (21) was performed and the results are shown in Fig. 8. As before the measured data are denoted by the circled points, and the theory, using Eq. (21) with $\alpha_T = 1$, is shown by the solid line. The quasi-steady theory, using the cascade correlations of Fig. 3, is shown as a dashed line. This prediction was obtained from Eq. (21) by setting $\chi = \chi_{ss}$ and $\rho C_{ax} \Xi_m \partial U/\partial t = 0$. Finally, a theoretical curve including unsteady loss but neglecting the kinetic energy of the flow within the passage, denoted by the dash-dot curve, was obtained by setting $\alpha_T = 1$ in Eq. (10) and suppressing the last term of Eq. (21). Figure 8 shows that unsteady terms must be included in the analysis to properly model the fluid dynamics of inlet distortion. It also shows that for the specific case examined here the unsteady kinetic energy term has a greater influence on the results than the unsteady loss. (The difference between the dashed and the dash-dot curves is the contribution of the unsteady loss, and the difference between the dash-dot and the solid curves is that of the unsteady kinetic energy within the blade passage.) However, it will be shown in a later section that the unsteady loss term has a significant effect on flow stability and rotating stall.

TWO-DIMENSIONAL FLOW FIELD ANALYSIS

The analytical model to predict the aerodynamic response of an isolated, high hub-tip ratio axial compressor blade row, subjected to an upstream velocity distortion, is based on the assumptions that (1) the flow field is incompressible and inviscid and (2) the inlet velocity distortion is independent of radial position. The second assumption allows the analysis to be developed in the two-dimensional cascade plane. This is shown schematically in Fig. 9, which represents the flow field ahead of and behind an axial compressor blade row, unwrapped tangentially and projected onto a two-dimensional plane. The lines ABC and DEF represent a common axial trace in the three-dimensional compressor system, and this correspondence imposes a periodic boundary condition on the flow; viz., it is required that any flow particle leaving (or entering) the region through line ABC must enter (or leave) the region through line DEF with the same vector velocity. A distorted inlet flow is prescribed along the inlet boundary AD, and a constant static exit pressure condition is imposed at exit boundary CF. The blade row represented by the line BE is modelled as a semi-actuator disk across which there is a change in the flow direction as well as a change in the total pressure.

The flow field upstream and downstream of the blade row will satisfy the incompressible, time-dependent, two-dimensional Euler equations of motion,

$$\frac{\partial U}{\partial t} + U \frac{\partial U}{\partial x} + V \frac{\partial U}{\partial y} = -\frac{1}{\rho} \frac{\partial p}{\partial x} \tag{22}$$

$$\frac{\partial V}{\partial t} + U \frac{\partial V}{\partial x} + V \frac{\partial V}{\partial y} = -\frac{1}{\rho} \frac{\partial p}{\partial y} \quad . \tag{23}$$

and the equation of continuity,

$$\frac{\partial U}{\partial x} + \frac{\partial V}{\partial y} = 0 \tag{24}$$

If

$$\zeta = \frac{\partial V}{\partial x} - \frac{\partial U}{\partial y} \tag{25}$$

is the normal component of vorticity, then these equations can be combined to yield the vorticity transport equation (cf. Ref. 11)

$$\frac{\partial \zeta}{\partial t} + U \frac{\partial \zeta}{\partial x} + V \frac{\partial \zeta}{\partial y} = 0 \tag{26}$$

For an inviscid flow upstream and downstream of the blade row this equation implies a constant vorticity along any material line in the flow, excluding the blade row itself. Equation (26) is hyperbolic which implies that

vorticity can only be created at the boundaries of the designated flow field. Thus, with reference to Fig. 9, vorticity can only be created along the inlet plane boundary, AD, the actuator disk, BE, and the exit plane boundary CF. In particular, the creation of vorticity associated with reverse flow at the actuator disk, BE, is admissible in this solution. This means that the rotating stall phenomenon, which can be accompanied by local regions of reverse flow, is not excluded from this analytical model. The creation of vorticity at this boundary is governed by the interactions of the flow field equations developed in this section and the pressure rise boundary condition across BE determined in an earlier section. It will be shown later that the specification of the form of the inlet distortion at the entrance plane AD provides the necessary information for the specification of vorticity along this boundary. It is not possible to establish any rational cirterion for the specification of vorticity at the exit plane. This would be necessary only if a region of reverse flow at the actuator disk BE extended downstream far enough to penetrate the boundary CF. Under these circumstances either the case under consideration could be regarded as invalid or the boundary CF could be moved further downstream to avoid the reverse flow region. However, in all of the cases considered herein there were no detectable regions of reverse flow and it is considered unlikely that such problems will arise in the vicinity of the exit plane boundary.

The assumption that the flow field is incompressible and two-dimensional in the cascade plane allows the introduction of a stream function, ψ, which is related to the axial and tangential velocity components by the equations

$$U = \frac{\partial \psi}{\partial y}, V = -\frac{\partial \psi}{\partial x} \tag{27}$$

A combination of Eqs. (25) and (27) yields the expression

$$\nabla^2 \psi = \frac{\partial^2 \psi}{\partial x^2} + \frac{\partial^2 \psi}{\partial y^2} = -\zeta \tag{28}$$

The final flow field equations that will be needed for this solution involve the relationships between the total pressure at any point in the flow field and the other fluid properties at that point. From Eqs. (22) through (25) (or from Ref. 11) these relationships take the form

$$\frac{\partial U}{\partial t} + \frac{\partial}{\partial x}\left(\frac{P_0}{\rho}\right) = V\zeta \tag{29}$$

$$\frac{\partial V}{\partial t} + \frac{\partial}{\partial y}\left(\frac{P_0}{\rho}\right) = -U\zeta \tag{30}$$

which are essentially the axial and tangential momentum equations.

A simultaneous solution of Eqs. (26) and (28) which satisfies the appropriate boundary conditions will yield the velocity field upstream and downstream of the blade row, and the total pressure field can be obtained by

integrating Eqs. (29) and (30). When these equations are combined with Eqs. (19) and (21) for the blade row pressure rise the result comprises the desired nonlinear, coupled set of equations, valid for large disturbances, and including nonlinear loss and unsteady flow effects.

NUMERICAL PROCEDURE AND BOUNDARY CONDITIONS

The numerical procedure employed in this study is a standard center differencing method for the stream function equation, (28), and Arkawa's vorticity conservation algorithm (Ref. 12) and the Crank-Nicholson scheme (Ref. 13) to solve Eq. (26). The usual procedure is to prescribe a distortion at $t = 0$ at the inlet plane, AD, and to maintain it at the inlet for all later times. This implies a tacit assumption that the inlet plane is far enough upstream to be unaffected by the presence of the blade row at BF. At each time step over $t \geq 0$ the propagation of the disturbance through the flow field is computed subject to a simultaneous satisfaction of all boundary conditions. The computation is terminated either when a steady state condition is achieved or, in the case of an unsteady downstream solution, when such a solution becomes periodic. (The latter is characteristic of rotating stall.) Each of the boundary conditions will now be described in detail.

Inlet Conditions

The circumferential distortion profile is prescribed at the inlet plane AD by specifying the functional form of the stream function,

$$\psi(x,y,t)\Big|_{x \text{ at } AD} = g(y,t) \tag{31}$$

Note that this specification is one-dimensional (i.e., independent of x at this point) and that it can have a time dependency. From Eqs. (28) and (31), the vorticity along AD can be computed using

$$\zeta(x,y,t)\Big|_{x \text{ at } AD} = -\frac{\partial^2 \psi(x,y,t)}{\partial y^2}\Big|_{x \text{ at } AD} = f(y,t) \tag{32}$$

Flow Periodicity

It was noted in an earlier section that flow entering (or leaving) along the line ABC must disappear (or reappear) in the same form and distribution along the line DEF. This is expressed by the periodicity conditions

$$\zeta(x,y,t)\Big|_{y \text{ at } DEF} = \zeta(x,y,t)\Big|_{y \text{ at } ABC} \tag{33}$$

and

$$\psi(x,y,t)\Big|_{y \text{ at } DEF} = \psi(x,y,t)\Big|_{y \text{ at } ABC} + Q^* \tag{34}$$

where Q^* is the axial flow rate through the entire flow field,

$$Q^* = 2\pi R_M U^* \tag{35}$$

where R_M is the mean radius of the annulus.

Pressure Rise Across Actuator Disk

The expression for the pressure rise across the actuator disk, based on unsteady blade passage characteristics, is given in Eq. (18). A comparable equation for total pressure across the blade row may be obtained by rewriting Eq. (30) in the form

$$\frac{\partial}{\partial y}\left(\frac{\overline{P}_{02}}{\rho}\right) - \frac{\partial}{\partial y}\left(\frac{P_{01}}{\rho}\right) = -\frac{\partial V_2}{\partial t} + \frac{\partial V_1}{\partial t} + U_2\zeta_2 - U_1\zeta_1 \tag{36}$$

When Eq. (18) is differentiated with respect to y it can be combined with Eq. (36) to eliminate the pressures, and the result is

$$\frac{1}{2}\frac{\partial}{\partial y}\left(q_1^2 x\right) + \frac{\partial}{\partial y}\left(c_{ax}\,\Xi_m\,\frac{\partial U}{\partial t}\right) = \frac{\partial V_2}{\partial t} - \frac{\partial V_1}{\partial t} + U\left(\zeta_1 - \zeta_2\right) \tag{37}$$

where $U = U_1 = U_2$ by continuity. Analogous to Eq. (20) (or from Fig. 2) we can write

$$V_2 = U\tan\beta_2\left(\beta_1\right) \tag{38}$$

so Eq. (37) finally becomes

$$\frac{\partial V_1}{\partial t} - \frac{\partial}{\partial t}\left(U\tan\beta_2\right) = -\frac{1}{2}\frac{\partial}{\partial y}\left(q_1^2 x\right) - c_{ax}\,\Xi_m\,\frac{\partial^2 U}{\partial y\,\partial t} + U\left(\zeta_1 - \zeta_2\right) \tag{39}$$

This equation relates the velocity field immediately upstream of the blade row to the change in vorticity across the blade row. It is expressed in

finite difference form by approximating the time derivatives by a forward difference scheme and the spatial terms by a central difference approximation.

Vorticity at Blade Row Exit Plane

A combination of Eqs. (27) and (28), evaluated at the blade row exit plane (station 2) yields

$$\zeta_2 = \frac{\partial V_2}{\partial x} - \frac{\partial U}{\partial y} \tag{40}$$

and again using Eq. (38),

$$\zeta_2 = \frac{\partial}{\partial x}\left(U \tan\beta_2\right) - \frac{\partial U}{\partial y} \tag{41}$$

which must be satisfied by the vorticity at the blade row exit plane.

Flow Field at Exit Plane

The final boundary condition states that the static pressure is constant along the flow field exit plane, CF. From Eq. (23) this is given by

$$\left[\frac{\partial V}{\partial t} + U\frac{\partial V}{\partial x} + V\frac{\partial V}{\partial y}\right]_{x \text{ at } CF} = 0 \tag{42}$$

COUPLED FLOW FIELD AND BLADE ROW ANALYSIS

The combination of flow field and blade passage solutions described in the previous two sections was programmed for the UARL UNIVAC 1108 digital computer and a number of cases were examined. In this portion of the study the system geometry and the loss and turning characteristics were identical to those in Ref. 7.

A cosine wave inlet velocity distortion was chosen for the first cases examined, given by the formula $(U-U^*)/U^* = -0.3\cos\theta$. It has a magnitude equal to 30 percent of the undistorted velocity (based on the circumferential axial velocity average, U^*) and is imposed $\frac{1}{2}$ blade row circumferences upstream of the blade row. This is shown as the dashed line in Fig. 10 for an inlet angle of $\beta_1 = 42$ deg. Also shown in this figure is the axial velocity distribution at the rotor inlet at a dimensionless time $t^* = 2.94$ after the imposition of the distortion. (Note that when $t^* \equiv \Omega t/2\pi = 1$ the rotor has made 1 revolution.) The same steady-state distribution was obtained for all values of t^* after the passage of the initial transient. This figure shows that the distortion pattern is attenuated axially and shifted circumferentially in the direction of rotation by the presence of the downstream blade row. At this inlet angle the rotor blade incidence angle is below the stall angle, $\beta_1 = 35$ deg, and no flow instability is present. (Note that the incidence angle can be defined as the difference between the blade row stagger angle and the inlet angle, $\alpha = \beta_1^* - \beta_1$. In this case $\beta_1^* = 63.5$

deg so $\beta_1 = 42$ deg in Fig. 9 corresponds to $\alpha = 21.5$ deg and the stalling angle $\beta_1 = 35$ deg is equivalent to $\alpha = 28.5$ deg.)

The effect of increasing incidence angle is shown in Figs. 11 through 13 for the same cosine wave distortion. In the cases examined here the flow rate was held constant and the wheel speed was increased. This has the effect of decreasing β_1 and, hence, increasing α. In Fig. 11 a 2 deg increase in incidence angle causes a significant flow instability to occur in the low velocity region (270 deg $< \theta <$ 360 deg), as evidenced by the lack of repeatability for the three values of t* selected for this figure. The instability appears to be attenuated as the high velocity region is approached, but the velocity profiles are not completely repeatable -- they merely exhibit similar behavior as the high velocity region is approached.

In Fig. 12, for $\alpha = 25.5$ deg, the unsteadiness is much more pronounced and now persists over a larger region of the circumference. It should be noted that the fluctuation in velocity at the blade row in the low velocity region is now of the same order of magnitude as the original velocity distortion. Specifically, note the change in the normalized axial velocity for $t^* = 2.42$ and $t^* = 2.90$ at $\theta = 270$ deg. As before, the unsteadiness appears to attenuate as the high velocity region is approached.

Finally, in Fig. 13, we have what appears to be a completely unsteady flow which persists over the entire circumference. Waves are formed at the inlet face which propagate nonuniformly in the direction of rotation but at a fraction (averaging $\frac{1}{2}$) of rotor speed, indicative of rotating stall. This

is shown in more detail in Fig. 14 which is a computer-generated plot for the same case as in Fig. 13. The horizontal axis is again circumferential position and the vertical axis is both normalized velocity and nondimensional time. The first curve (at the bottom of the figure), denoted "cosine wave" is the original distortion imposed $\frac{1}{2}$ circumference upstream of the blade row. The remaining curves are the velocity profiles at the blade row inlet taken at a series of values of t* which increases from bottom to top. This pseudo-three-dimensional figure shows the formation of a velocity deficiency in the low velocity region which propagates in the direction of rotation (to the left) and attenuates as it passes through the high velocity region, only to reappear and strengthen again in the low velocity region.

It should be noted that in Ref. 7, which analyzed this blade row geometry with no inlet distortion, rotating stall first occurred at $\beta_1 = 35$ deg or $\alpha = 28.5$ deg, which is a higher incidence angle than any shown here. With the imposition of a 30 percent distortion the first evidence of rotating stall is found in Fig. 12 for $\alpha = 25.5$ deg and, to some extent in Fig. 11 for $\alpha = 23.5$ deg. Thus, the presence of an inlet distortion serves to reduce the equivalent steady-state incidence angle at which rotating stall occurs, in this case by as much as 5 degrees. The analysis predicts the same effect as that observed in rotor experiments; namely, the stable operating range of the rotor is reduced by the presence of an inlet distortion.

The influence of the unsteady kinetic energy term within the blade passage is examined in Figs. 15 and 16 by setting $C_{ax}/2\pi R_M = 0$. This has

the effect of eliminating the entire kinetic energy term in Eq. (21). The same upstream cosine wave distortion was used as in Fig. 10. A comparison of Figs. 10 and 15 for $\alpha = 21.5$ deg and Figs. 13 and 16 for $\alpha = 27.5$ deg shows that the absence of the kinetic energy term has virtually no effect on the predicted velocity profile at both low and high incidence angles. This is in apparent contradiction with the results described earlier in the section entitled Application of Blade Row Analysis, in which the kinetic energy effect was dominant. However, in the earlier results the rotor blade row was preceded by inlet guide vanes which retarded the circumferential attenuation of the relatively sharp edged distortion. Hence, the factor $\partial U/\partial t$ in Eq. (21) was important in this application of the analysis and, accordingly, so was the kinetic energy. In the present case the cosine wave has a much smaller circumferential gradient to begin with, and the axial attenuation further reduces the influence of the velocity time derivative, $\partial U/\partial t$.

Next, a steeper and narrower distortion pattern was examined, shown by the dashed line in Fig. 17. In this case the wheel speed, Ω, and the average axial velocity, U^*, were the same as in Fig. 10. This time the distortion cosine wave extended only over the range 90 deg $< \theta <$ 270 deg, and was flat elsewhere (i.e., this was a half-wave 180 deg distortion). This is

given by

$$\frac{U-U^*}{U^*} = \begin{cases} 0.15\,, & 0 \le \theta \le 90\,\text{deg}\,,\ 270\,\text{deg} \le \theta \le 360\,\text{deg} \\ 0.3\cos 2\left(\theta - \frac{\pi}{2}\right) - 0.15\,, & 90\,\text{deg} \le \theta \le 270\,\text{deg} \end{cases} \tag{43}$$

This waveform and the full circumference wave used earlier both have the same circumferentially averaged mean value of axial velocity and both have the same peak-to-peak amplitude.

It is readily seen that this distortion, extending over only 180 deg of the circumference, has a higher harmonic frequency content than the previous distortion which extended over the full 360 deg of circumference. In Fig. 17, for $t^* = 2.94$, the peak-to-peak distortion at the blade row inlet (solid curve) is smaller in magnitude than in Fig. 10. It is believed that this amplitude attenuation takes place because the inertia of the flow field prevents a rapid response to the higher harmonics. In effect, the fluid inertia behaves as a low pass filter, permitting the response to follow the lower harmonics of the upstream distortion but suppressing the response at the higher harmonics. As before, the distortion at the blade row inlet is shifted in the direction of rotation.

Figures 18 and 19 show the effect of increasing incidence. Again the flow instability or rotating stall develops in the low velocity region and attenuates in the high velocity region, with the effect becoming more pronounced as α is increased. However, this time the instability is unable to grow as before around the entire circumference, even at the highest

incidence angle, probably because of the inertia effects cited above.

Finally, in Fig. 20, the effect of suppressing the kinetic energy term is again examined for this higher relative frequency by setting $C_{ax}/2\pi R_M = 0$. The upper curve is for low incidence, $\alpha = 21.5$ deg, and the lower curve is for high incidence, $\alpha = 27.5$ deg. A comparison of the upper part of Fig. 20 with Fig. 17 for $\alpha = 21.5$ deg, and the lower part of Fig. 20 with Fig. 19 for $\alpha = 27.5$ deg again shows a minimal influence of the kinetic energy term on velocity response. Here it is believed that, although the initial distortion is steeper than before, the axial attenuation that takes place at the blade row inlet reduces the contribution of the factor $\partial U/\partial t$ to approximately the same level as in the full circumference distortion.

RESULTS AND CONCLUSIONS

The results of this investigation are as follows:

1) A nonlinear, large disturbance theory has been developed which couples, interactively, the flow through the blade passages of a turbomachine blade row and the flow through the surrounding field.

2) The theory predicts the degradation of the stable operating range of an isolated rotor due to the presence of an upstream distortion.

3) Use of the uncoupled blade passage theory shows that for a sharp-edged, unattenuated distortion the kinetic energy term is dominant.

4) Use of the coupled theory and cosine wave distortions shows that the kinetic energy term is less important because of the reduced circumferential gradient of velocity and that the dominant effects arise from the inclusion of total pressure loss and from the coupling between blade row pressure changes and flow field vorticity changes. However, if sharp velocity gradients exist, the kinetic energy term would probably contribute strongly in these regions of high gradient.

The conclusions reached in the course of this study are as follows:

1) The predicted degradation of the stable operating range of a single blade row due to the presence of an axial distortion is of the same order as the available measured results from multistage machines.

2) At low incidence angles an upstream axial distortion is attenuated spatially as it approaches a blade row, and the flow through the blade row

remains stable.

3) At high incidence angles an upstream axial distortion having a circumferential wave length equal to the annular circumference will produce disturbances in the region of the blade row which are amplified axially in the low velocity region and attenuated in the high velocity region.

4) These disturbances propagate circumferentially as a rotating stall in the direction of rotation at approximately one-half the wheel speed of the rotor.

5) An upstream axial distortion which occupies one-half the annular circumference will be attenuated more than the longer wave length distortion because the inertia of the fluid restricts the response capabilities of the fluid system to higher harmonics.

6) For the one-half circumference distortion at high incidence angles the tendency for the creation of rotating stall cells is reduced.

REFERENCES

1. Carta, F. O.: Analysis of Unsteady Aerodynamic Effects on an Axial-Flow Compressor Stage with Distorted Inflow. Project SQUID Technical Report UARL-1-PU, July 1972.

2. Rannie, W. D. and F. E. Marble: Unsteady Flows in Axial Turbomachines. Communication Aux Journées Internationales de Sciences Aéronautiques, Paris, May 1957.

3. Dunham, J.: Non-Axisymmetric Flows in Axial Compressors. Mechanical Engineering Science Monograph No. 3, Institution of Mechanical Engineers, 1965.

4. Callahan, G. M.: Attenuation of Inlet Flow Distortion Upstream of Axial Flow Compressors. Ph.D. Dissertation, Lehigh University, 1968.

5. Shapiro, A. H.: The Dynamics and Thermodynamics of Compressible Fluid Flow, Vol. I. The Ronald Press Company, New York, 1953.

6. Stenning, A. H., A. R. Kriebel, and S. R. Montgomery: Stall Propagation in Axial-Flow Compressors. NACA TN 3580, June 1956.

7. Nagano, S. and H. Takata: Nonlinear Analysis of Rotating Stall. Institute of Space and Aeronautical Science, University of Tokyo, Report No. 449, April 1970.

8. Henderson, R. E. and J. H. Horlock: An Approximate Analysis of the Unsteady Lift on Airfoils in Cascade. Transactions ASME, Journal of Engineering for Power, Vol. 94, October 1972, pp. 233 - 240.

REFERENCES (Continued)

9. Johnson, I. A. and R. O. Bullock, ed: Aerodynamic Design of Axial Flow Compressors. NASA SP-36, 1965. (See section by W. H. Roudebush and S. Lieblein, Viscous Flow in Two-Dimensional Cascades.)

10. Nagano, S., Y. Machida, and H. Takada: Dynamic Performance of Stalled Blade Rows. Presented at the Tokyo Joint International Gas Turbine Conference and Products Show, Tokyo, Japan, October 1971. Japan Society of Mechanical Engineers paper JSME 11.

11. Milne-Thomson, L. M.: Theoretical Hydrodynamics. The Macmillan Company, New York, 4th ed., 1960.

12. Arkawa, A.: Computational Design for Long-Term Numerical Integration of the Equations of Fluid Motion: Two-Dimensional Incompressible Flow. Part I. Journal of Computational Physics, Vol. I, 1966, pp. 119-143.

13. Richtmyer, R. D. and K. W. Morton: Difference Methods for Initial-Value Problems. Interscience Publishers, New York, 2nd ed., 1967.

LIST OF SYMBOLS

A	Area, ft^2
C_{ax}	Axial component of blade chord, ft
f	Functional form of vorticity, (ft/sec)/ft
g	Functional form of stream function, ft^2/sec
$\bar{n}$	Unit normal vector
p	Static pressure, lb/ft^2
P_o	Total pressure, lb/ft^2
ΔP_o	Total pressure loss, lb/ft^2
q	Resultant velocity, ft/sec
Q	Flow rate through blade passage, ft^3/sec
Q^*	Axial flow rate through entire flow field, ft^3/sec
R_M	Mean radius of blade row annulus, ft
t	Time, sec
t^*	Dimensionless time, $= \Omega t/2\pi$
U	Axial velocity, ft/sec
U^*	Circumferential average of Axial velocity, ft/sec
v	Volume, ft^3
V	Tangental velocity, ft/sec
x	Axial coordinate, ft
y	Tangential coordinate, ft
α	Cascade incidence angle, $= \beta_1^* - \beta_1$, deg

LIST OF SYMBOLS (Continued)

α_T	Dimensionless time constant
β_1, β_2	Inlet and exit flow angles, deg
β_1^*	Cascade stagger angle, deg
ζ	Vorticity, (ft/sec)/ft
θ	Circumferential coordinate, rad or deg
ξ	Local flow angle within blade passage, rad
ξ_{metal}	Local angle of blade camber line, rad
Ξ_m	Chordwise average of blade camber line angle
ρ	Fluid density, lb sec^2/ft^4
σ	Stall angle parameter, ratio of instantaneous incidence angle to stall angle
τ	Tangential gap, ft
χ	Unsteady loss parameter
χ_{ss}	Steady-state loss parameter
ψ	Stream function, ft^2/sec
Ω	Rotor wheel speed, rad/sec

Special symbols, superscripts and subscripts

∇^2	Laplacian operator
$\overline{(\ )}$	Gap average
$(\ )_1$	Blade row inlet plane
$(\ )_2$	Blade row exit plane

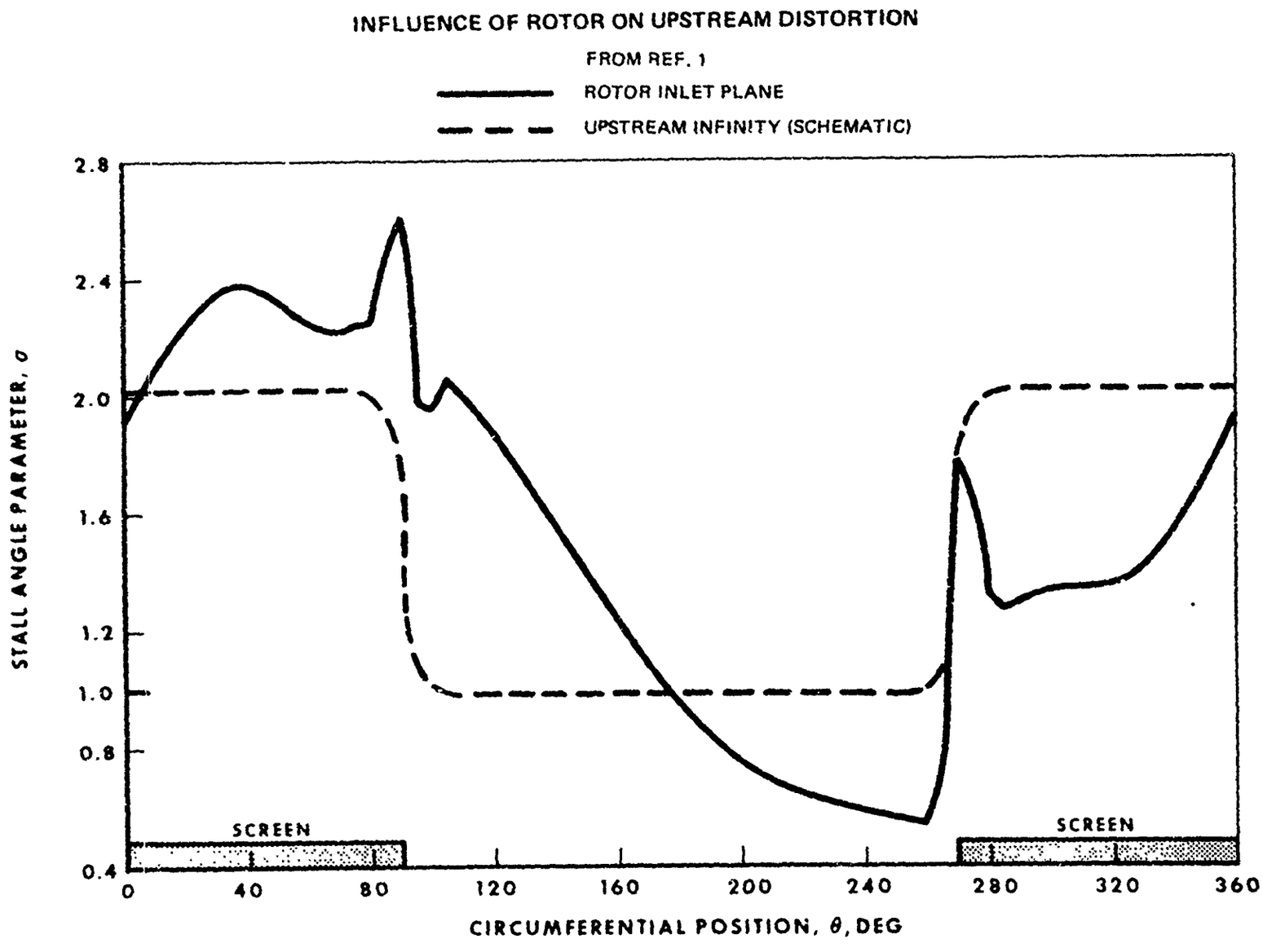
INFLUENCE OF ROTOR ON UPSTREAM DISTORTION
FROM REF. 1
ROTOR INLET PLANE
UPSTREAM INFINITY (SCHEMATIC)
STALL ANGLE PARAMETER, σ
2.8
2.4
2.0
1.6
1.2
1.0
0.8
0.4
SCREEN
SCREEN
0
40
80
120
160
200
240
280
320
360
CIRCUMFERENTIAL POSITION, θ, DEG

FIG. 1

FIG. 2

BLADE ROW COORDINATE SYSTEM AND FLOW PARAMETERS

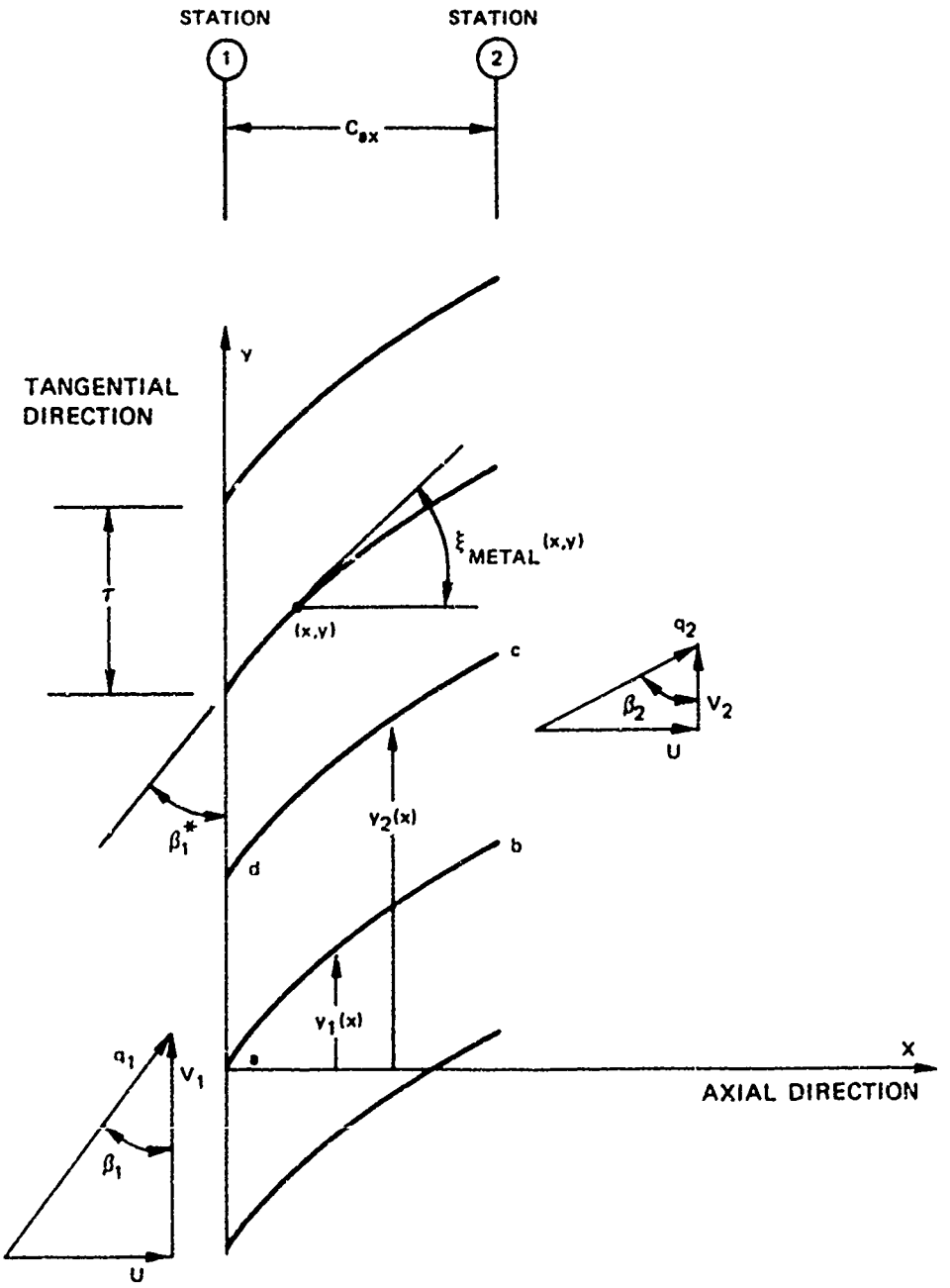

FIG. 3

STEADY–STATE LOSS AND TURNING CORRELATIONS
FOR ROTOR AND STATOR BLADE ROWS

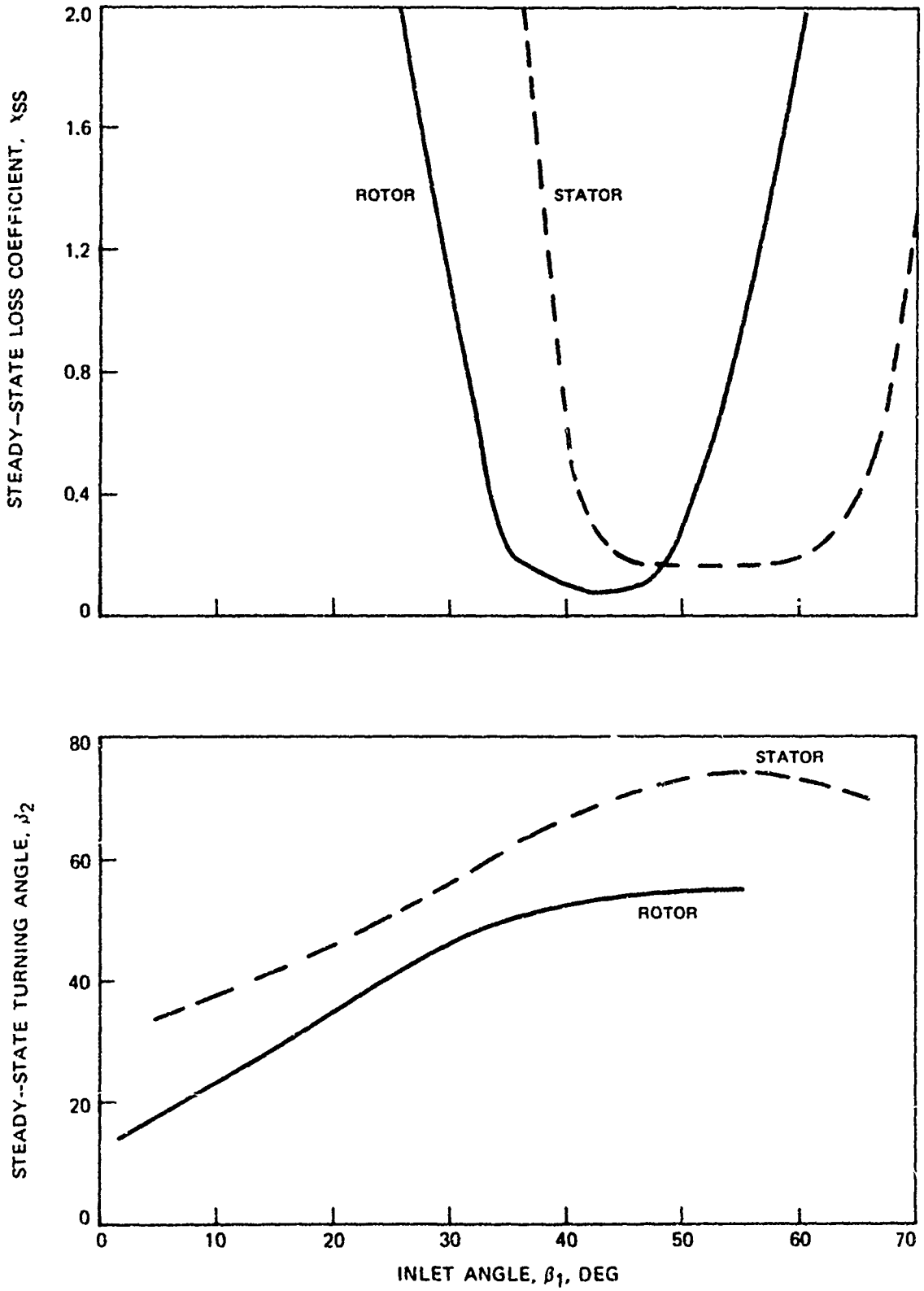

CIRCUMFERENTIAL STATIC PRESSURE PROFILE AT OUTER DIAMETER
FOR 180 DEG DISTORTION EXTENT – MIDFLOW CONDITION

$P_{ref.}$ = 415.1 IN. H_2O

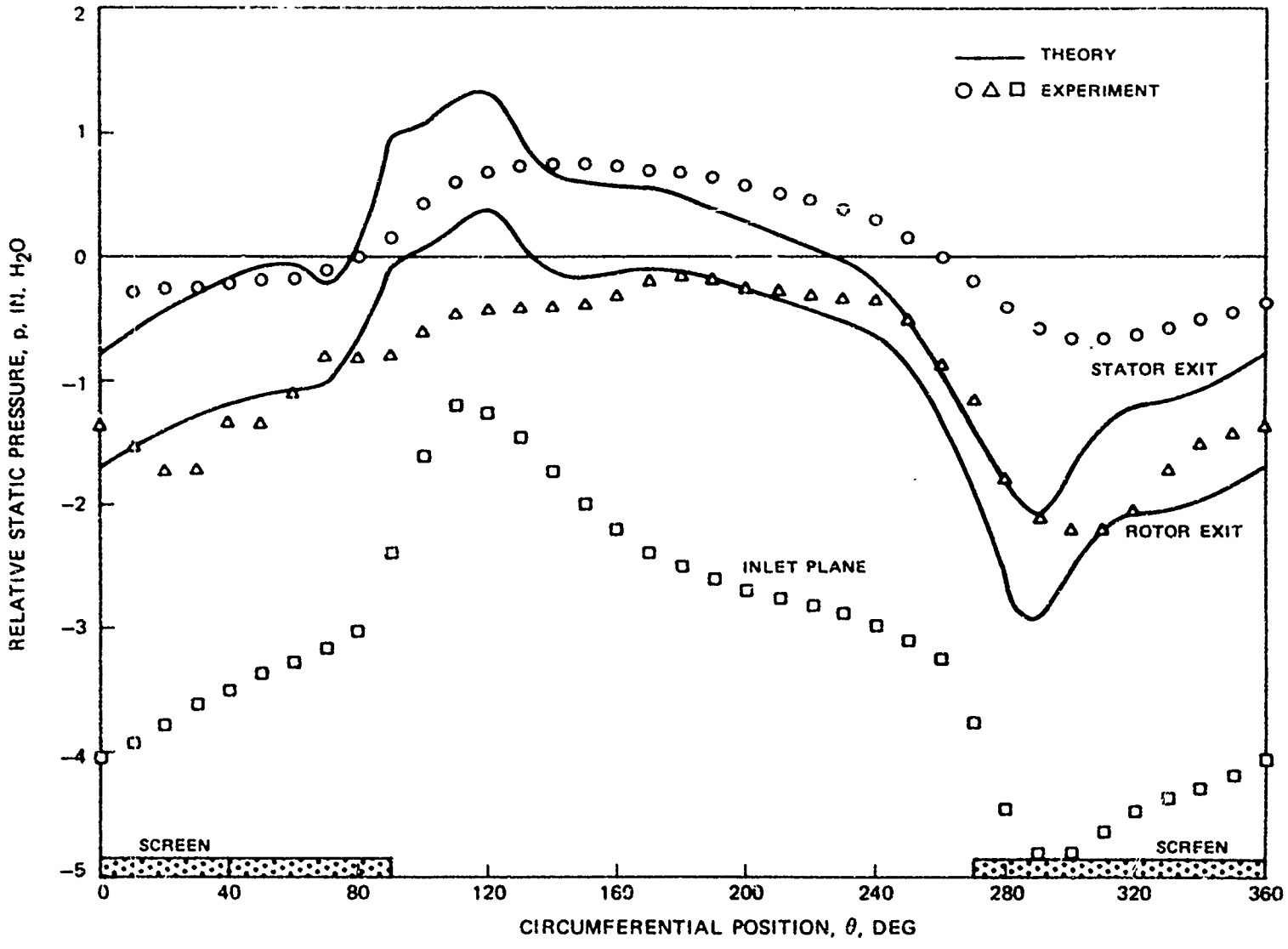

FIG. 4

CIRCUMFERENTIAL STATIC PRESSURE PROFILE AT OUTER DIAMETER FOR 180 DEG DISTORTION EXTENT – PEAK PRESSURE CONDITION

$P_{ref.}$ = 404.3 IN H_2O

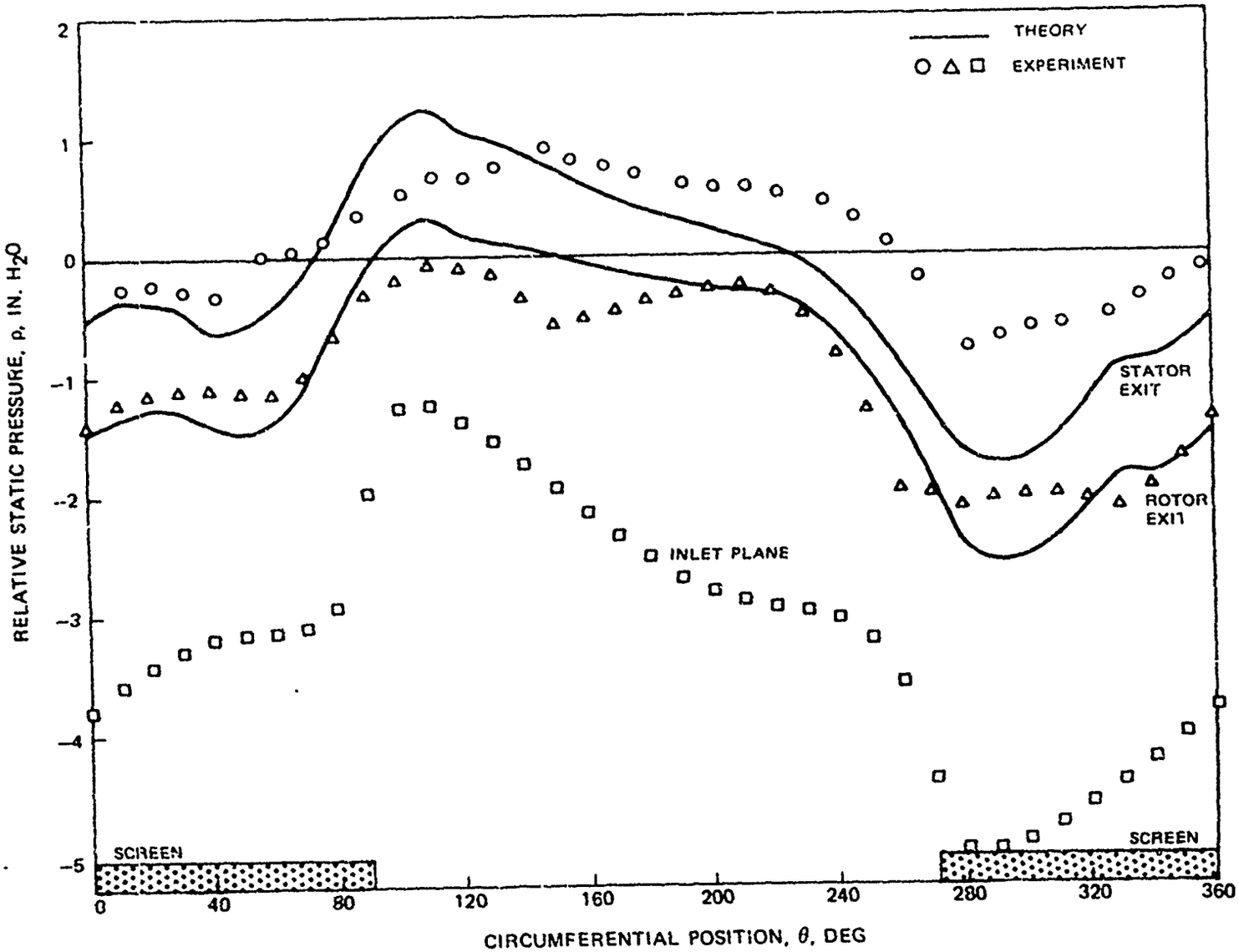

FIG. 5

CIRCUMFERENTIAL STATIC PRESSURE PROFILE AT OUTER DIAMETER FOR 180 DEG DISTORTION EXTENT – NEAR SURGE

$P_{ref.}$ = 414.8 IN. H_2O

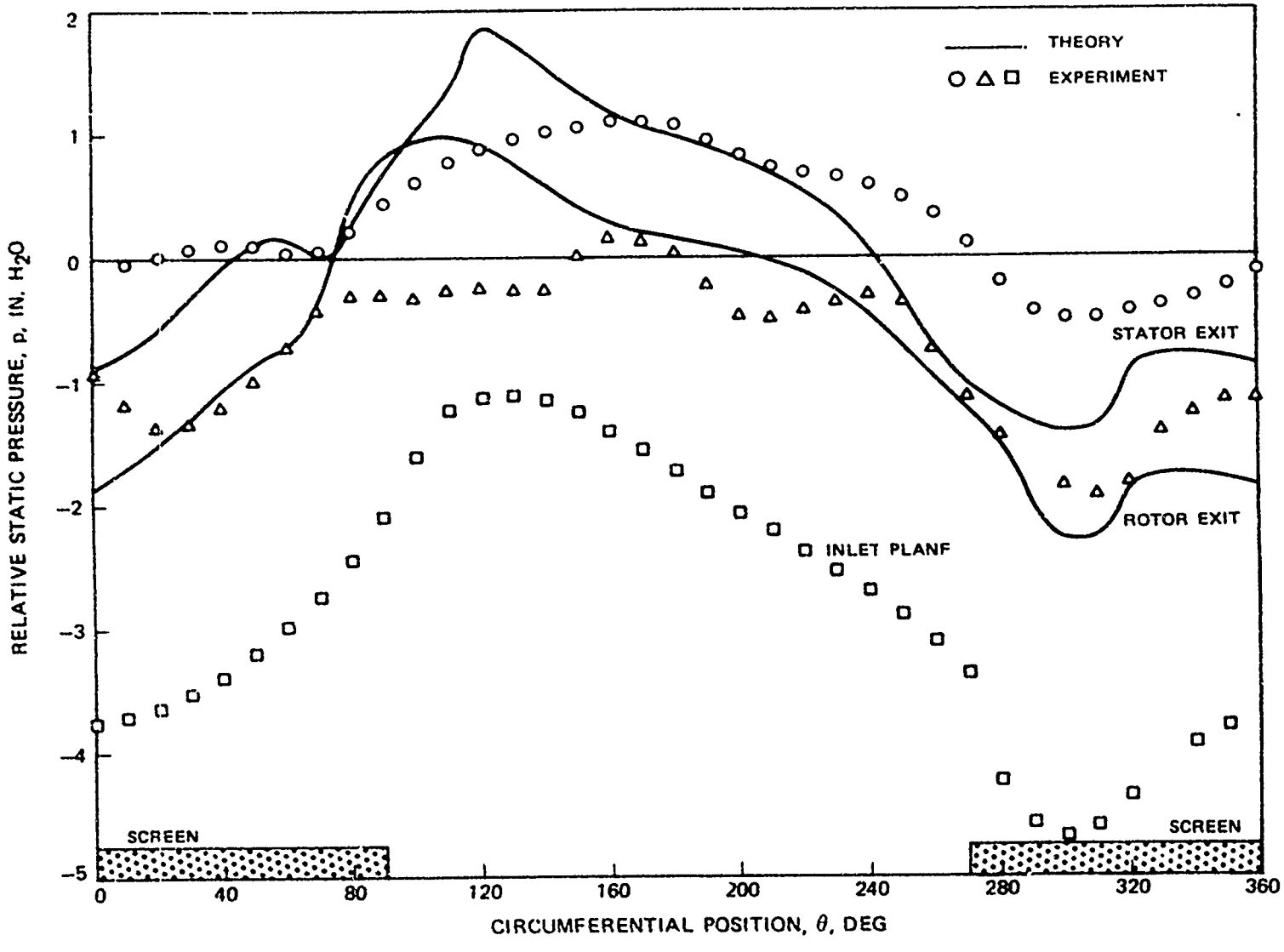

FIG. 6

COMPARISON BETWEEN PREDICTED AND MEASURED MID–ANNULUS STATIC PRESSURE AT ROTOR EXIT PLANE FOR 180 DEG DISTORTION EXTENT – PEAK PRESSURE CONDITION

$P_{ref.}$ = 404.3 IN. H_2O

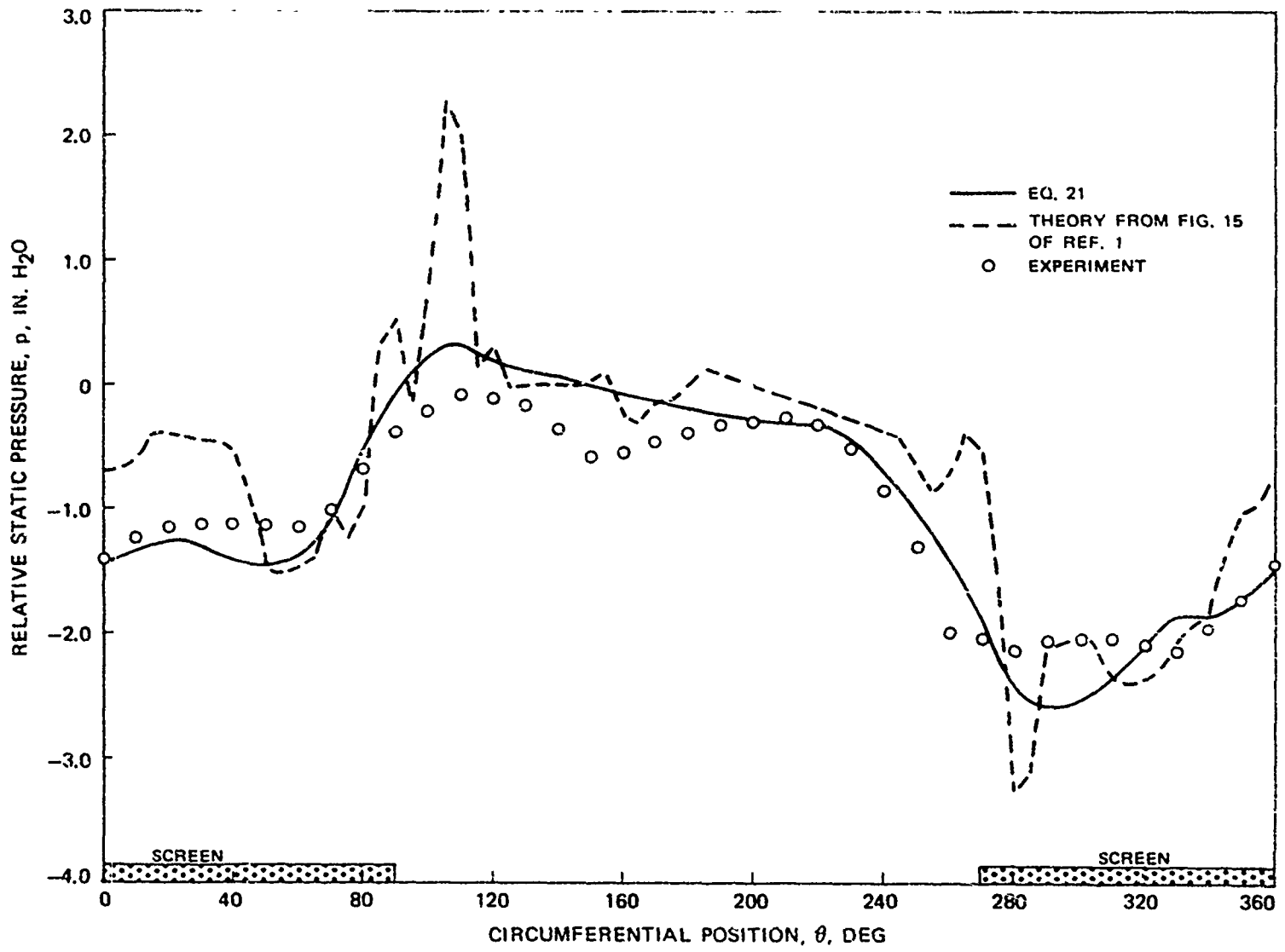

FIG. 7

EFFECT OF UNSTEADY LOSS AND UNSTEADY BLADE PASSAGE KINETIC ENERGY ON PRESSURE PREDICTION FOR PEAK PRESSURE CONDITION

(THEORY BASED ON CASCADE CORRELATION)

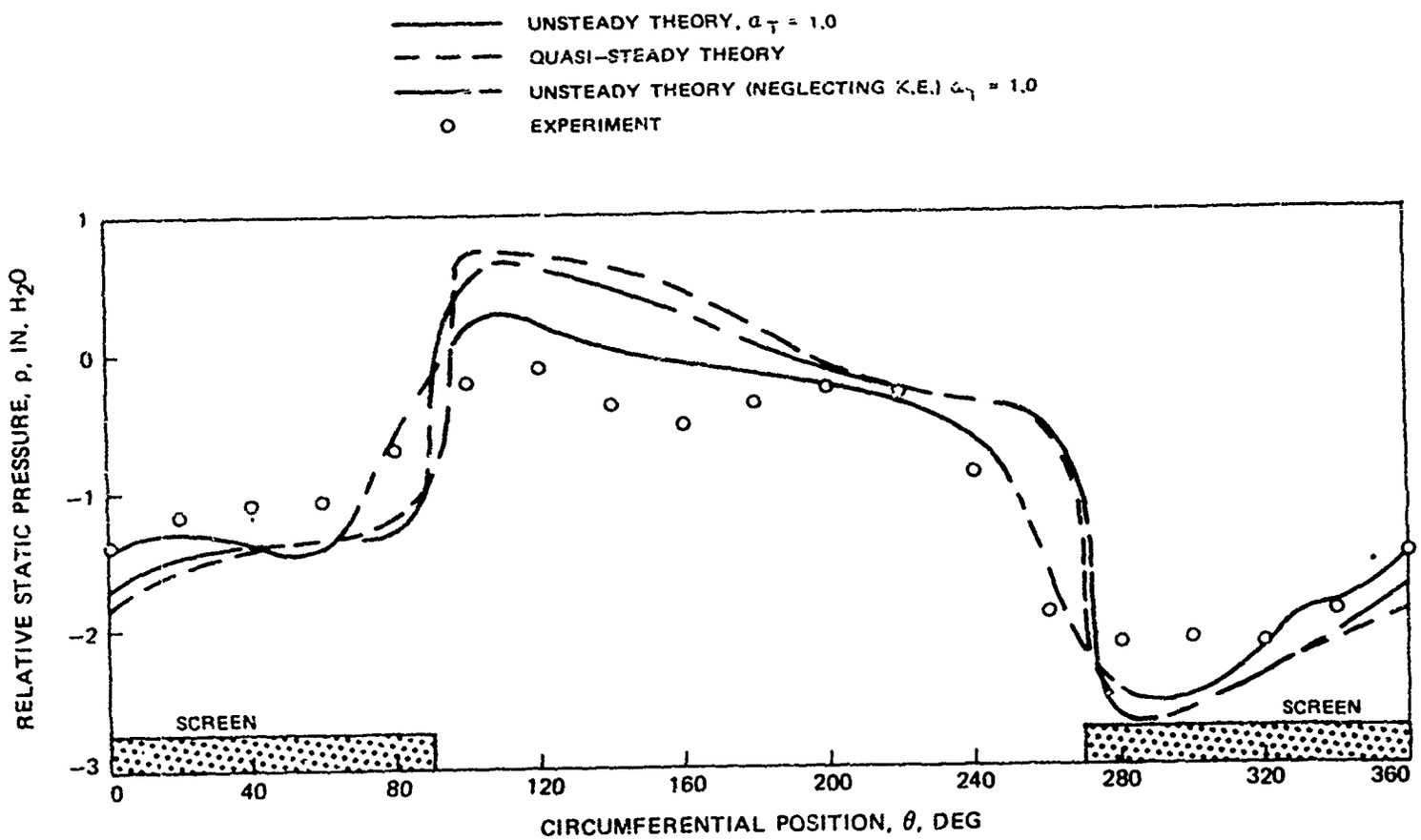

FIG. 8

45

SCHEMATIC DIAGRAM OF COMPRESSOR FLOW FIELD WITH SEMI–ACTUATOR DISK REPRESENTATION OF BLADE ROW

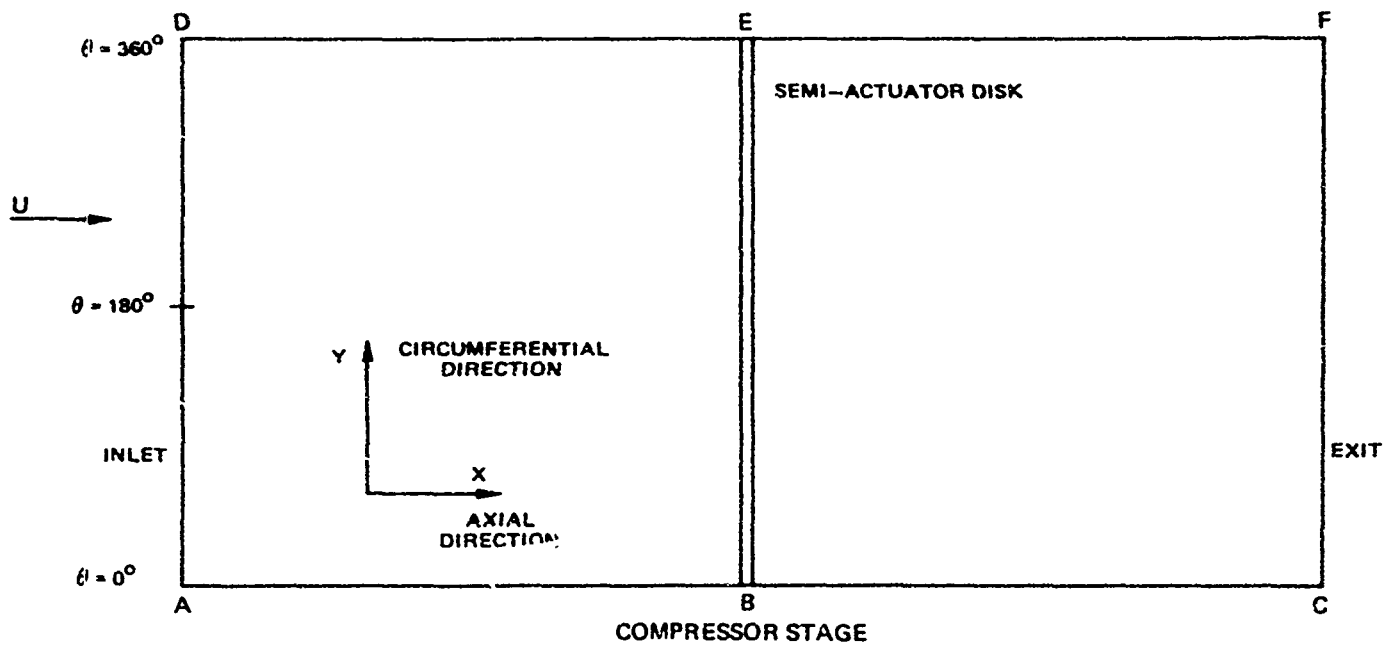

FIG. 9

FIG. 10

EFFECT OF COUPLING ON 360 DEG COSINE WAVE DISTORTION INCLUDING KINETIC ENERGY TERM FOR $\beta_1 = 42$ DEG

$\Omega = 21.5$ DEG

$\frac{C_{ax}}{2\pi R_M} = .01789$

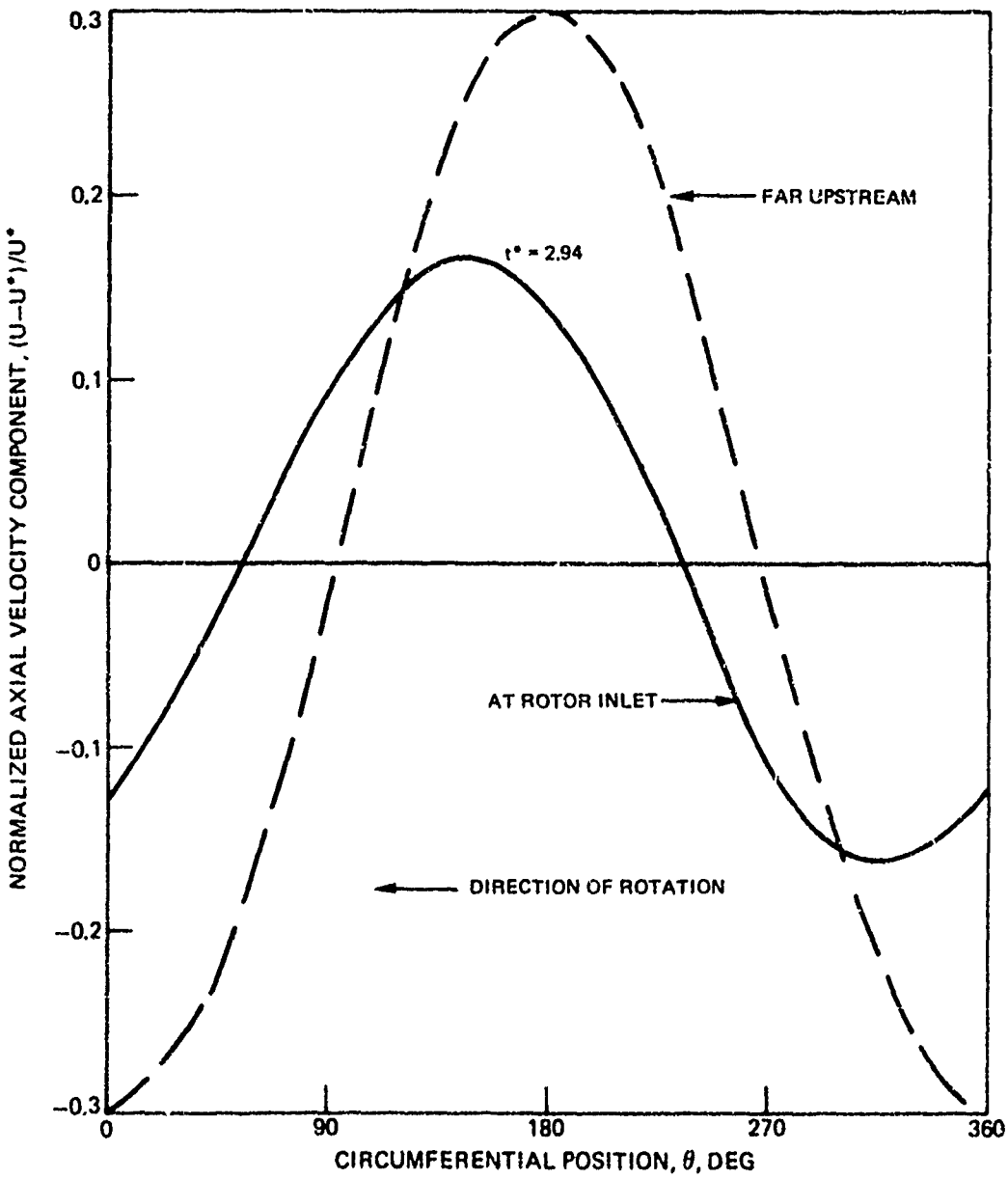

FIG. 11

EFFECT OF COUPLING ON 360 DEG COSINE WAVE DISTORTION INCLUDING KINETIC ENERGY TERM FOR β_1 = 40 DEG

α = 23.5 DEG

$$\frac{C_{ax}}{2\pi R_M} = .01789$$

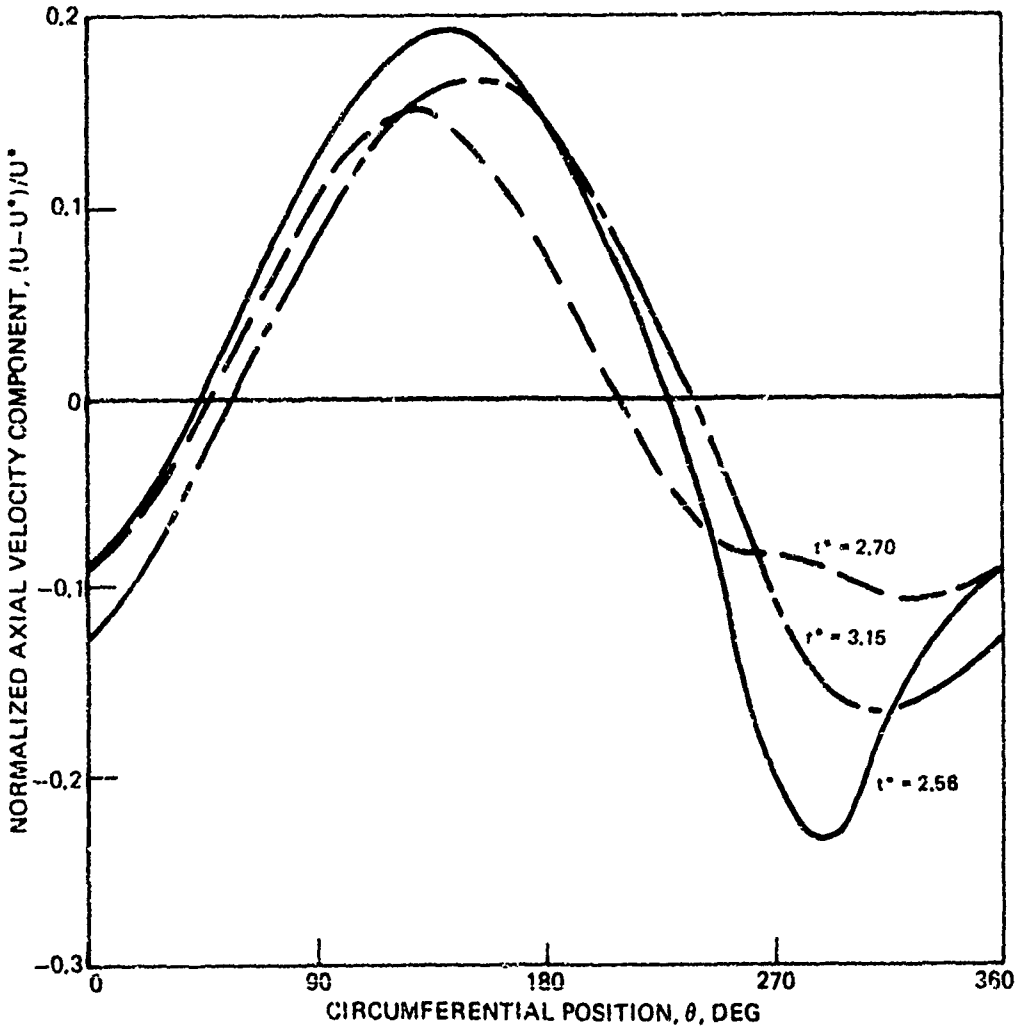

FIG. 12

EFFECT OF COUPLING ON 360 DEG COSINE WAVE DISTORTION INCLUDING KINETIC ENERGY TERM FOR β_1 = 38 DEG

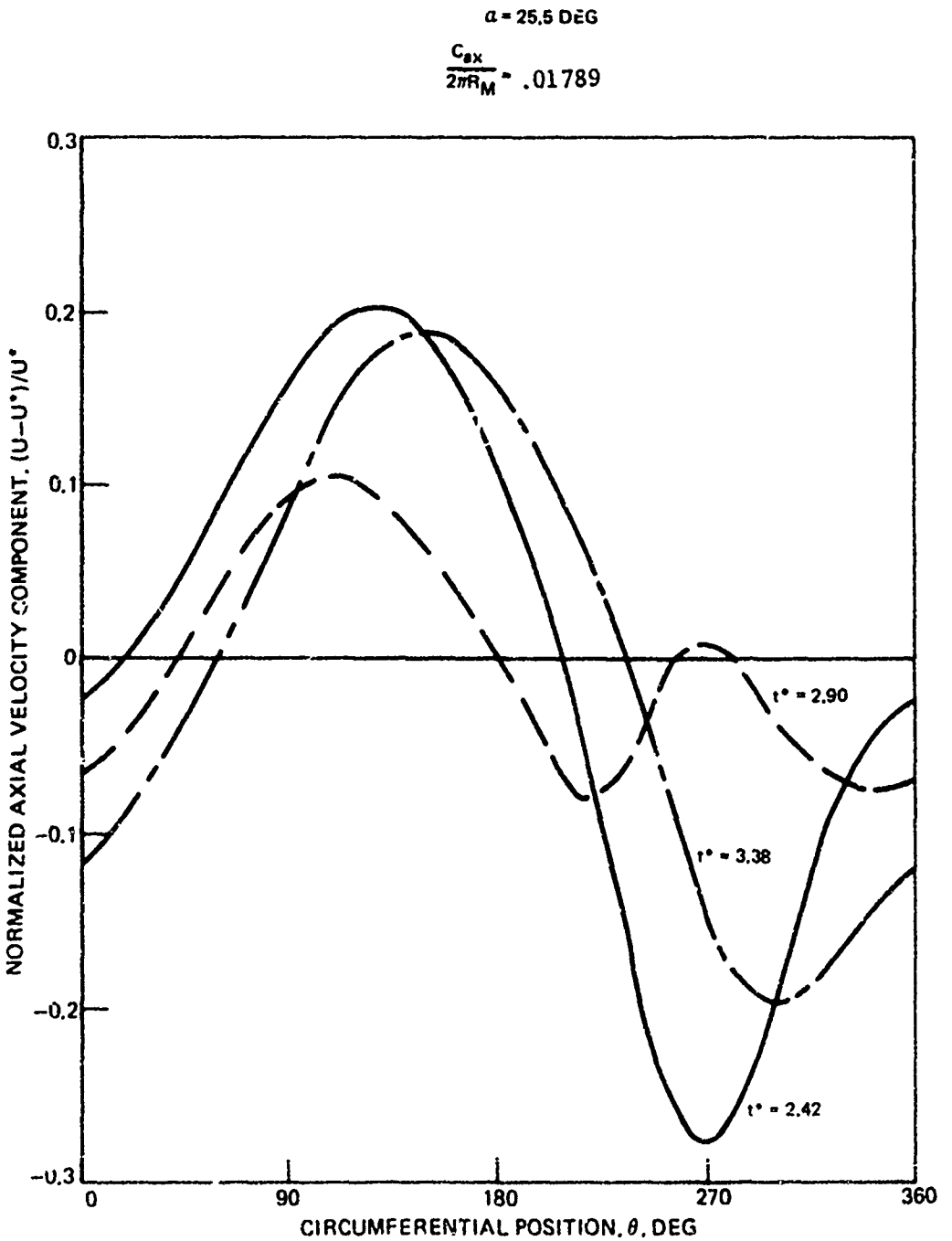

FIG. 13

EFFECT OF COUPLING ON 360 DEG COSINE WAVE DISTORTION INCLUDING KINETIC ENERGY TERM FOR β_1 = 36 DEG

α = 27.5 DEG

$\frac{C_{ax}}{2\pi R_M}$ = .01789

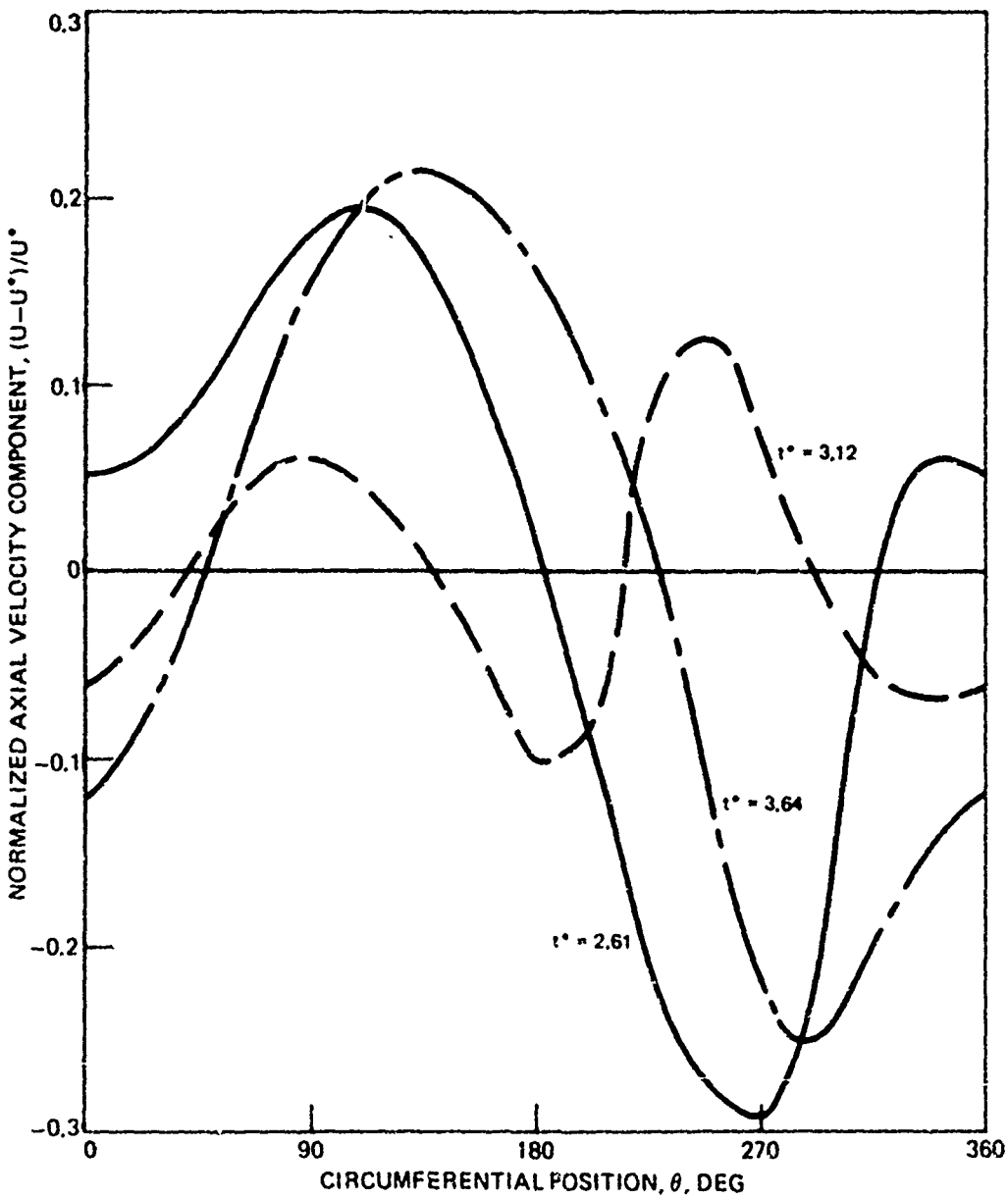

FIG. 14

PROPAGATION OF ROTATING STALL USING FULLY COUPLED SOLUTION FOR 360 DEG COSINE WAVE DISTORTION, β_1 = 36 DEG

$\frac{C_{ax}}{2\pi R_M} = .01789$

α = 27.5 deg DEG

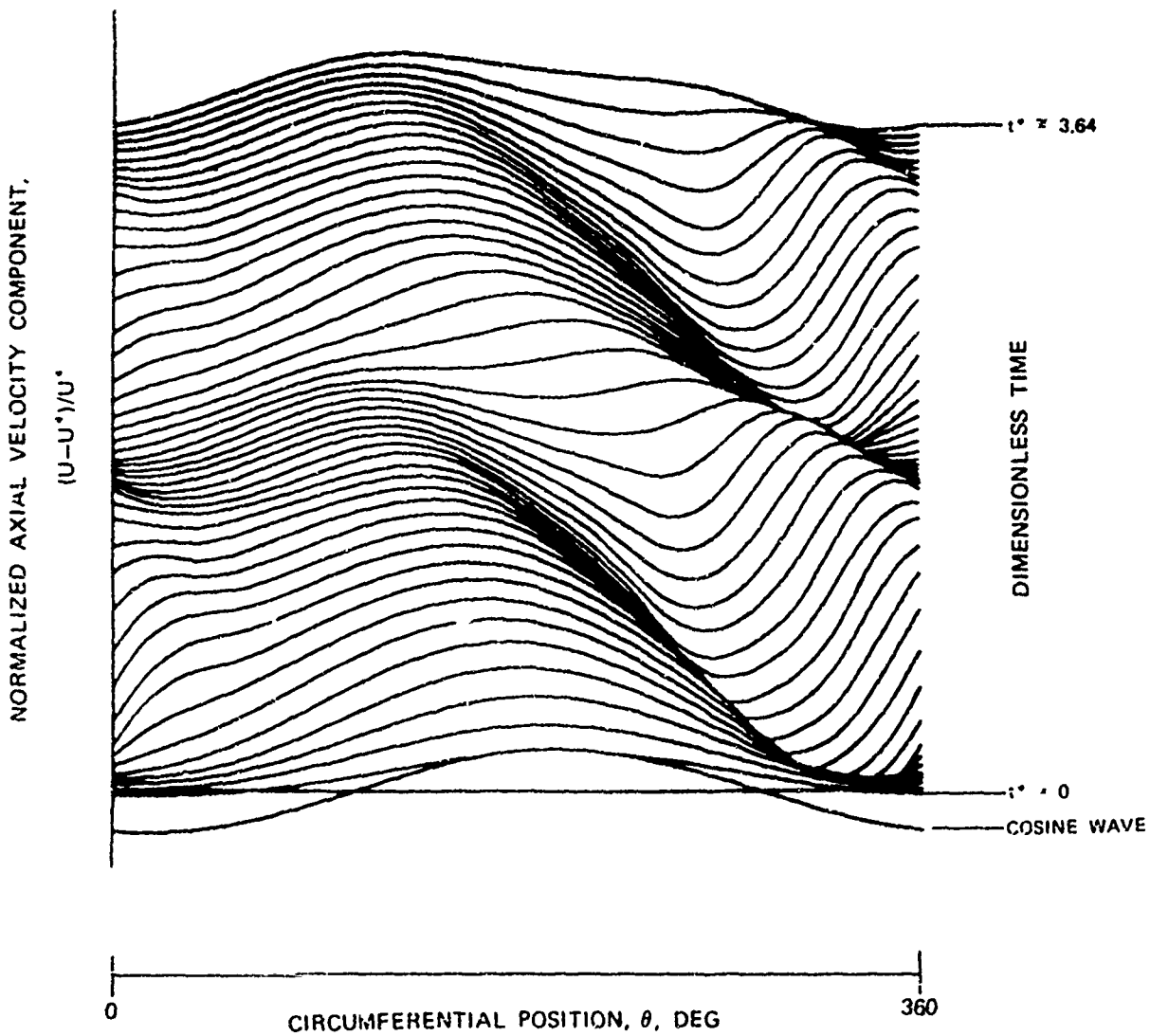

FIG. 15

EFFECT OF COUPLING ON 360 DEG COSINE WAVE DISTORTION WITH KINETIC ENERGY TERM SUPPRESSED FOR β_1 = 42 DEG

α = 21.5 DEG

$$\frac{C_{ax}}{2\pi R_M} = 0$$

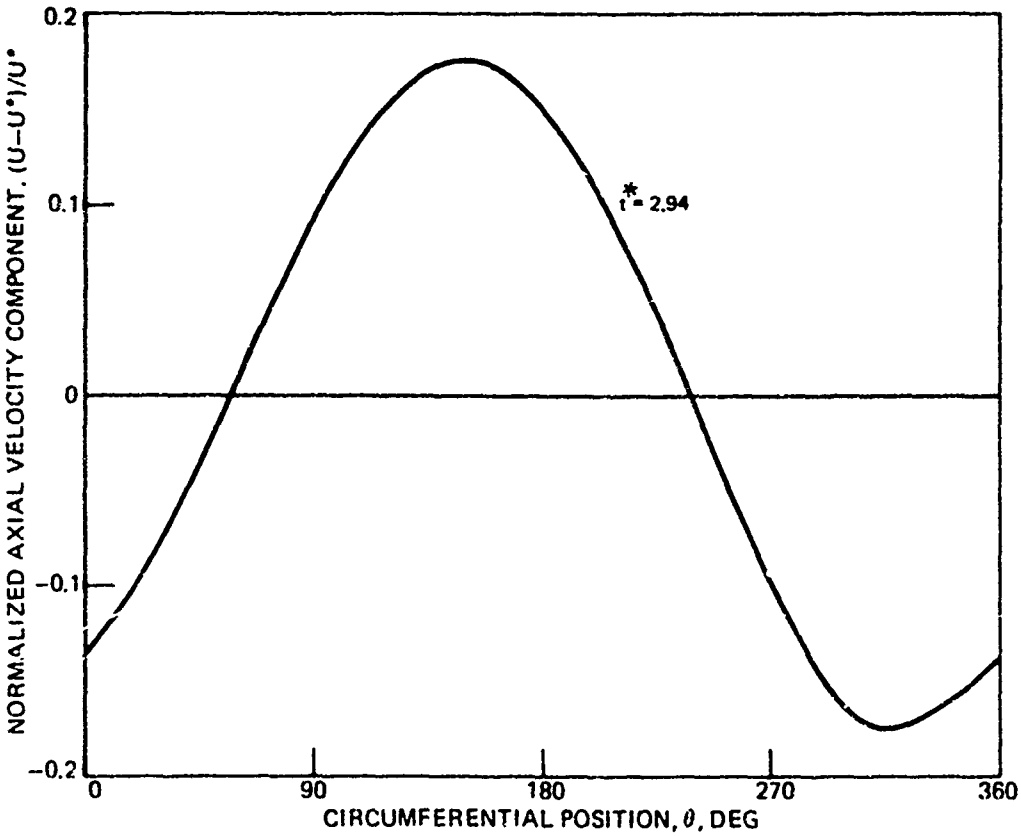

FIG. 16

EFFECT OF COUPLING ON 360 DEG COSINE WAVE DISTORTION WITH KINETIC ENERGY TERM SUPPRESSED FOR β_1 = 36 DEG

α = 27.5 DEG

$\frac{C_{ax}}{2\pi R_M} = 0$

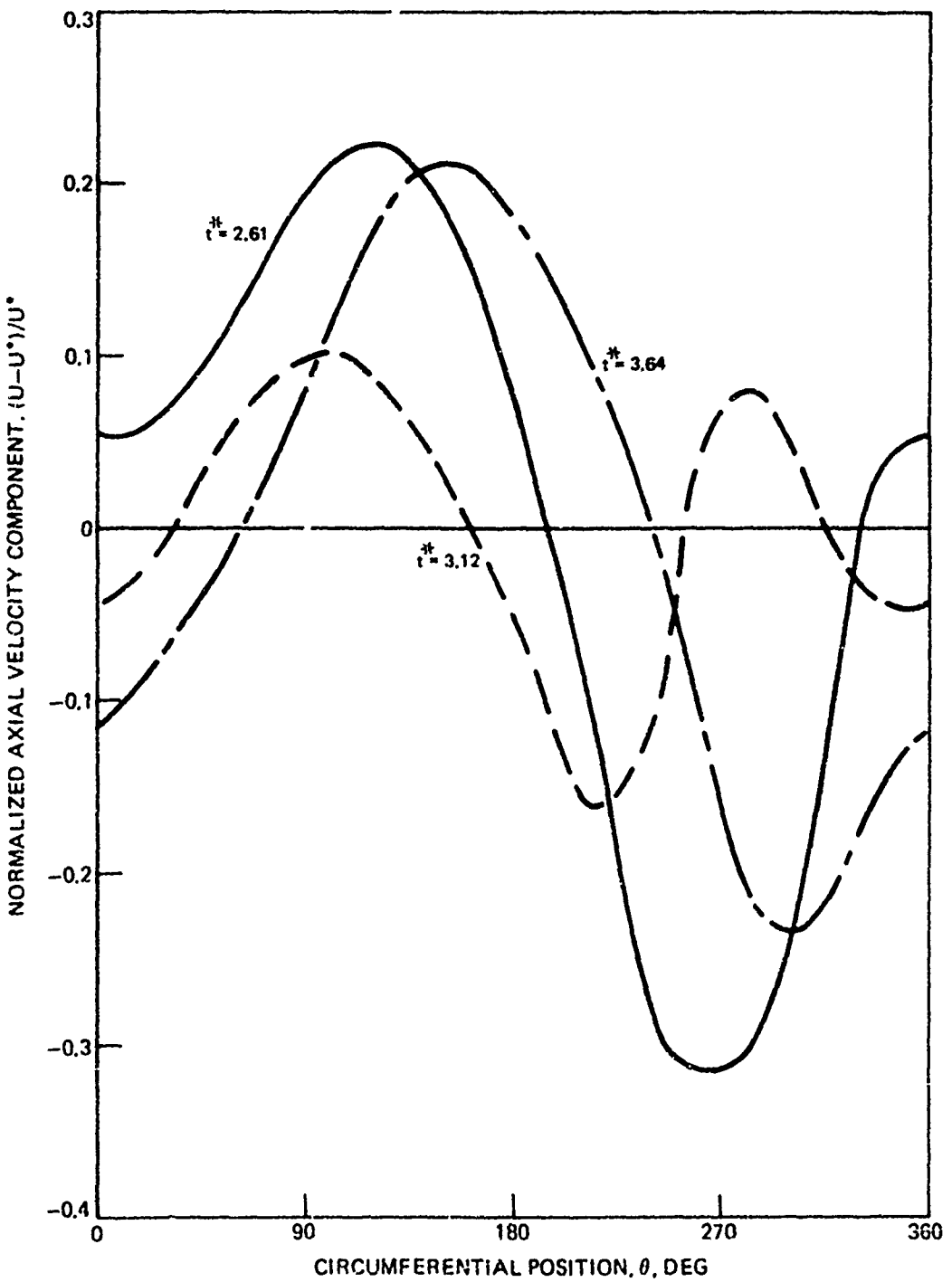

FIG. 17

EFFECT OF COUPLING ON 180 DEG COSINE WAVE DISTORTION INCLUDING KINETIC ENERGY TERM FOR β_1 = 42 DEG

α = 21.5 DEG

$\frac{C_{ax}}{2\pi R_M}$ = .01789

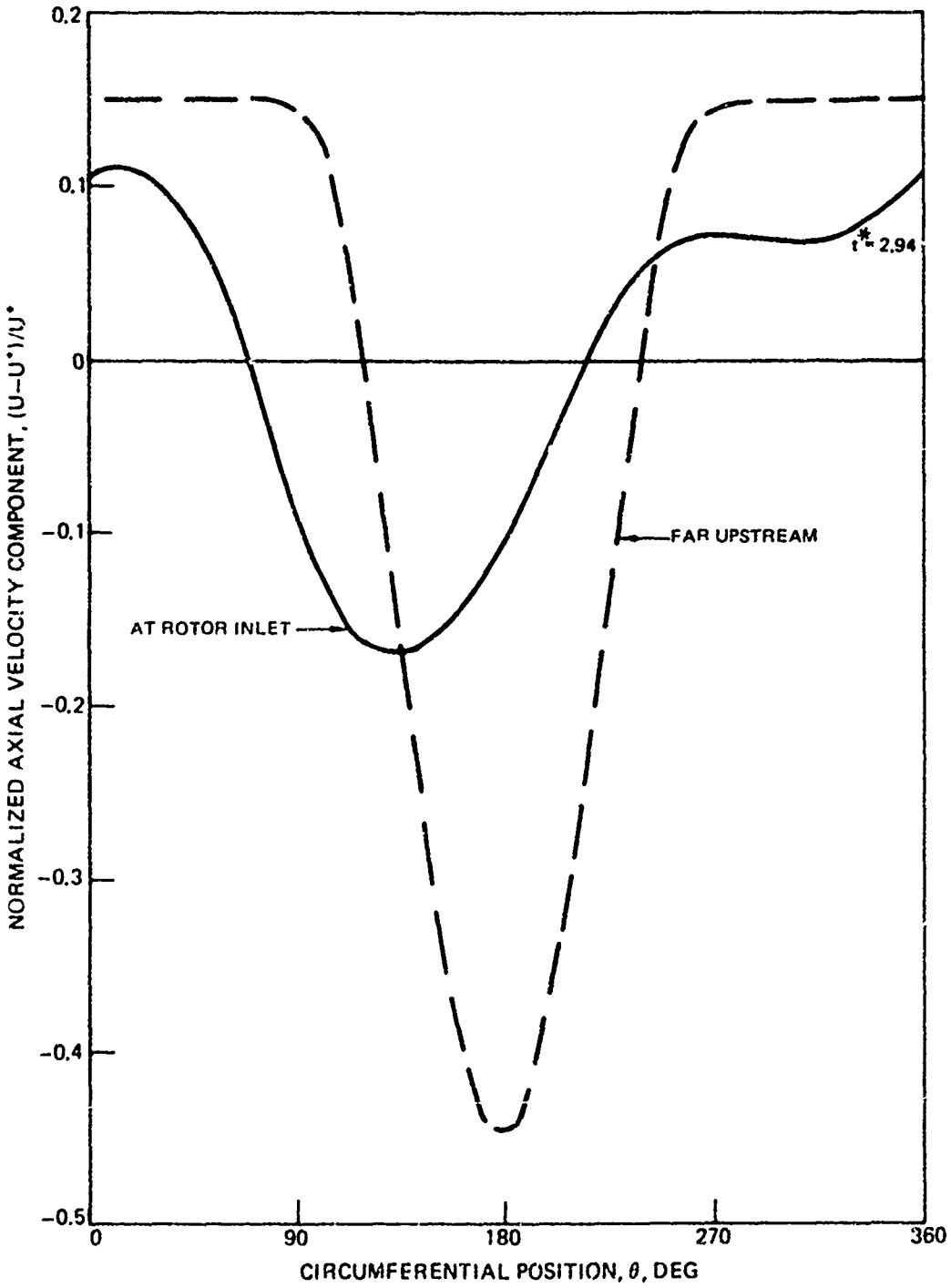

FIG. 18

EFFECT OF COUPLING ON 180 DEG COSINE WAVE DISTORTION INCLUDING KINETIC ENERGY TERM FOR β_1 = 40 DEG AND β_1 = 38 DEG

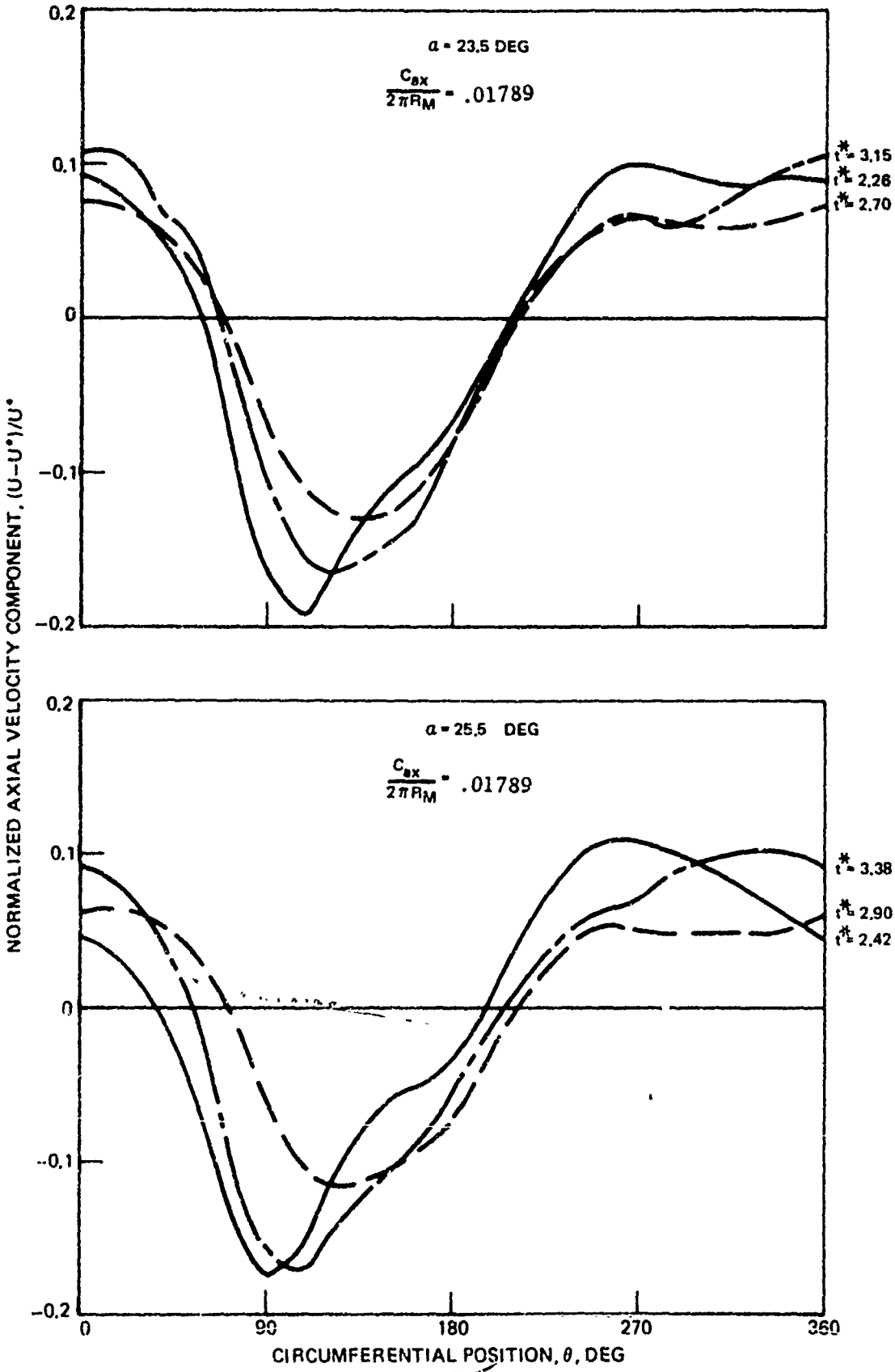

FIG. 19

EFFECT OF COUPLING ON 120 DEG COSINE WAVE DISTORTION INCLUDING KINETIC ENERGY TERM FOR β_1 = 36 DEG

α = 27.5 DEG

$\frac{C_{ax}}{2\pi R_M}$ = .01789

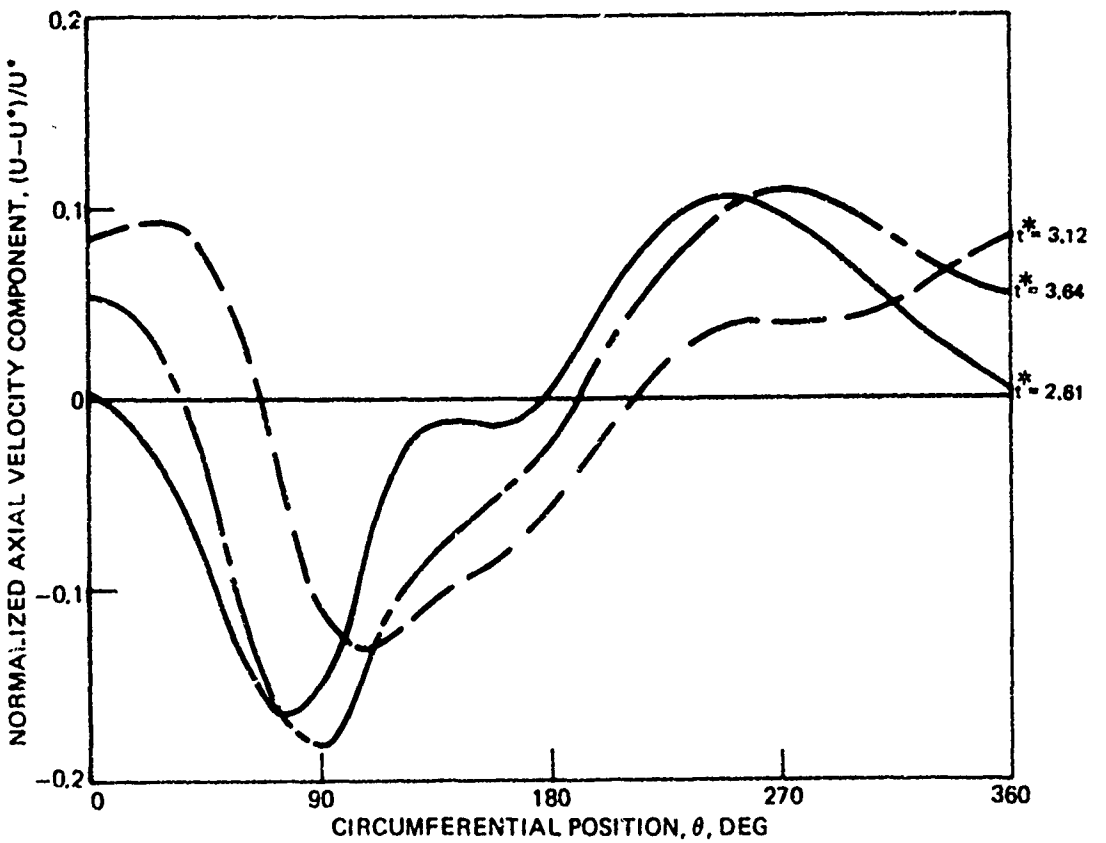

FIG. 20
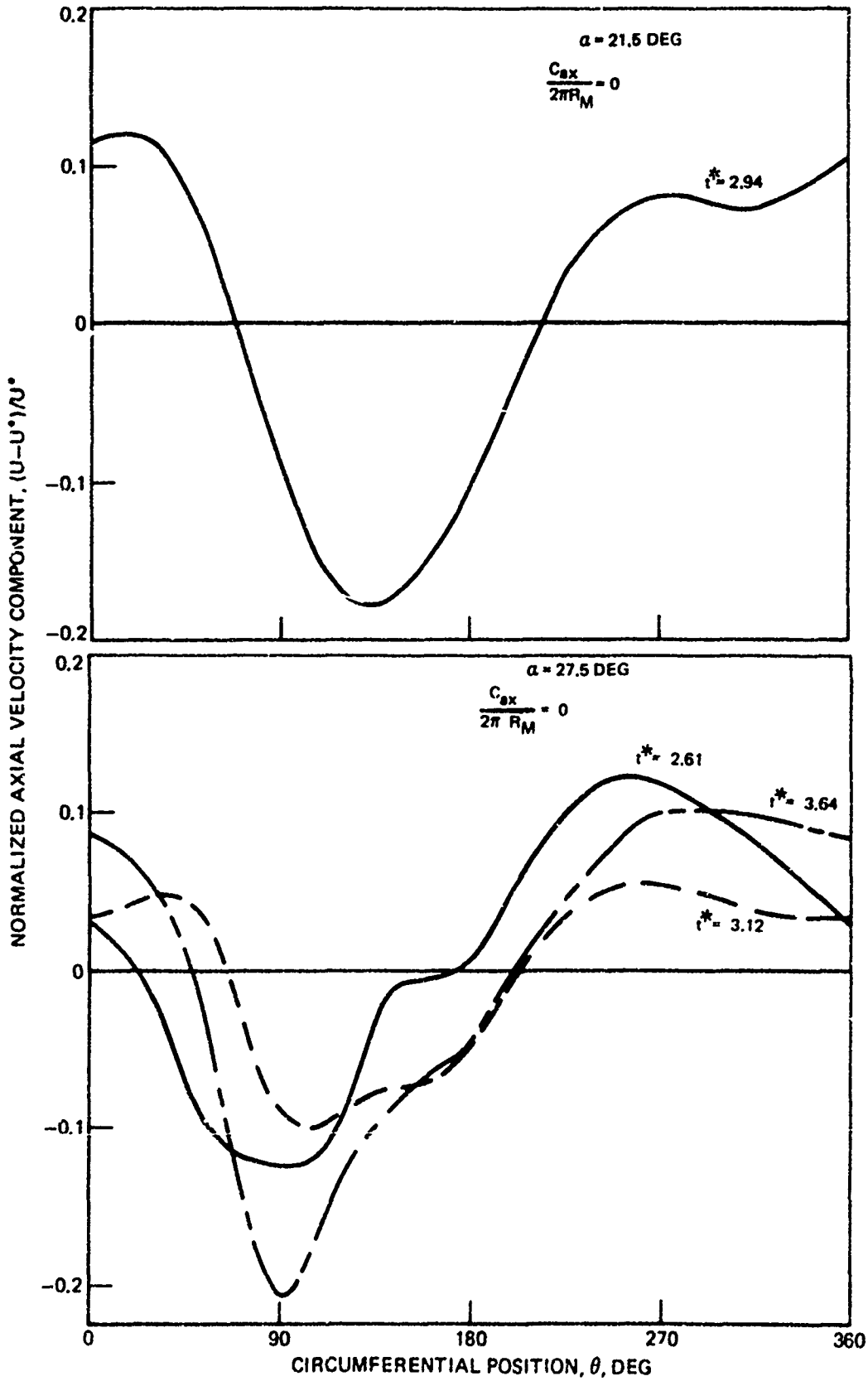
EFFECT OF COUPLING ON 180 DEG COSINE WAVE DISTORTION WITH KINETIC ENERGY TERM SUPPRESSED FOR β_1 = 42 DEG AND β_1 = 36 DEG